Monthly Notices of the ROYAL ASTRONOMICAL SOCIETY

MNRAS **500,** 3254–3274 (2021) doi:10.1093/mnras/staa3336
Advance Access publication 2020 October 28

The completed SDSS-IV extended Baryon Oscillation Spectroscopic Survey: large-scale structure catalogues and measurement of the isotropic BAO between redshift 0.6 and 1.1 for the Emission Line Galaxy Sample

Anand Raichoor,[1★] Arnaud de Mattia,[2] Ashley J. Ross,[3] Cheng Zhao,[1] Shadab Alam,[4] Santiago Avila,[5,6] Julian Bautista,[7] Jonathan Brinkmann,[8] Joel R. Brownstein,[9] Etienne Burtin,[2] Michael J. Chapman,[10,11] Chia-Hsun Chuang,[12] Johan Comparat,[13] Kyle S. Dawson,[9] Arjun Dey,[14] Hélion du Mas des Bourboux,[9] Jack Elvin-Poole,[3] Violeta Gonzalez-Perez,[7,15] Claudio Gorgoni,[1] Jean-Paul Kneib,[1,16] Hui Kong,[3] Dustin Lang,[11,17] John Moustakas,[18] Adam D. Myers,[19] Eva-Maria Müller,[20] Seshadri Nadathur,[7] Jeffrey A. Newman,[21] Will J. Percival,[10,11,17] Mehdi Rezaie,[22] Graziano Rossi,[23] Vanina Ruhlmann-Kleider,[2] David J. Schlegel,[24] Donald P. Schneider,[25,26] Hee-Jong Seo,[22] Amélie Tamone,[1] Jeremy L. Tinker,[27] Rita Tojeiro,[28] M. Vivek,[25,29] Christophe Yèche[2,24] and Gong-Bo Zhao[7,30,31]

Affiliations are listed at the end of the paper

Accepted 2020 October 17. Received 2020 October 16; in original form 2020 May 19

ABSTRACT

We present the Emission Line Galaxy (ELG) sample of the extended Baryon Oscillation Spectroscopic Survey from the Sloan Digital Sky Survey IV Data Release 16. We describe the observations and redshift measurement for the 269 243 observed ELG spectra, and then present the large-scale structure catalogues, used for the cosmological analysis, and made of 173 736 reliable spectroscopic redshifts between 0.6 and 1.1. We perform a spherically averaged baryon acoustic oscillations (BAO) measurement in configuration space, with density field reconstruction: the data two-point correlation function shows a feature consistent with that of the BAO, the BAO model being only weakly preferred over a model without BAO ($\Delta\chi^2 < 1$). Fitting a model constrained to have a BAO feature provides a 3.2 per cent measurement of the spherically averaged BAO distance $D_V(z_{\rm eff})/r_{\rm drag} = 18.23 \pm 0.58$ at the effective redshift $z_{\rm eff} = 0.845$.

Key words: galaxies: distances and redshifts – dark energy – distance scale – large-scale structure of Universe – cosmology: observations.

1 INTRODUCTION

The acceleration of the expansion of the Universe discovered about 20 yr ago (Riess et al. 1998; Perlmutter et al. 1999) set a key milestone in cosmology history: current observations can be accounted for with the ΛCDM standard model, but at the cost of introducing a dark energy component, making up today ∼70 per cent of the energy content of the Universe. Around the same time, the SDSS collaboration (York et al. 2000) initiated spectroscopic observations to study large-scale structures (LSSs), which allows one to constrain the geometry of the Universe with the Baryonic Acoustic Oscillations (BAO, Eisenstein & Hu 1998) and the growth of structures with redshift space distortion (RSD, Kaiser 1987).

Since then, the SDSS has become a key experiment for the BAO, one of the most powerful cosmological probes (see Weinberg et al. 2013, for a review). The SDSS first measured the distance-redshift relation with 5 per cent precision at $z = 0.35$ (Eisenstein et al. 2005) from 45 000 Luminous Red Galaxies (LRGs, Eisenstein et al. 2001). It was the first BAO detection along with the 2dF Galaxy Redshift Survey (Colless et al. 2003; Cole et al. 2005). The BOSS survey (2008–2014, Dawson et al. 2013) from the SDSS-III (Eisenstein et al. 2011) then massively observed 1.5 million LRGs and 160 000 quasars (QSOs), leading to a state-of-the-art 1–2 per cent precision measurement of the cosmological distance scale for redshifts $z < 0.6$ (Alam et al. 2017) and $z = 2.5$ (Delubac et al. 2015; Bautista et al. 2017). The Extended Baryon Oscillation Spectroscopic Survey (eBOSS, 2014–2020, Dawson et al. 2016) of the SDSS-IV (Blanton et al. 2017) observed nearly one million objects to complement the BOSS survey in the $0.6 < z < 2.2$ redshift range. eBOSS observed LRGs at $0.6 < z < 1.0$ (Prakash et al. 2016), Emission Line Galaxies at $0.6 < z < 1.1$ (ELGs, Raichoor et al. 2017), and QSOs at $0.9 < z < 3.5$ (Myers et al. 2015; Palanque-Delabrouille et al. 2016).

We present in this paper the eBOSS/ELG spectroscopic observations from the final release from SDSS-IV eBOSS Data Release 16 (DR16; Ahumada et al. 2020), along with the construction of the LSS catalogues, and the spherically averaged BAO measurement from

★ E-mail: anand.raichoor@epfl.ch

those. The LSS catalogues are also used in de Mattia et al. (2020) and Tamone et al. (2020) to analyse the ELG anisotropic clustering. ELGs are star-forming galaxies with strong emission lines – noticeably the [O II] doublet emitted at (λ3727, λ3729 Å), allowing a spectroscopic redshift ($z_{\rm spec}$) measurement in a reasonable amount of exposure time, as there is no need to significantly detect the continuum. This observational feature, combined with their abundance at $z \sim 0.5$–2 due to the high star formation density of the Universe then (e.g. Lilly et al. 1996; Madau, Pozzetti & Dickinson 1998; Madau & Dickinson 2014), makes them a promising tracer for LSSs surveys. The WiggleZ experiment (2006–2011, Drinkwater et al. 2010) was the first ELG BAO survey. Now eBOSS paves the way for the next-generation LSS surveys, which will heavily rely on the ELGs in the $0.5 \lesssim z \lesssim 2$ range, as PFS[1] (Sugai et al. 2012; Takada et al. 2014), DESI[2] (DESI Collaboration 2016a,b), *Euclid* (Laureijs et al. 2011), and *WFIRST*[3] (Doré et al. 2018). Indeed, this eBOSS/ELG sample has already been used for several analyses, which strengthen our understanding of ELGs at $z \sim 1$: exploring their physical content (Gao et al. 2018; Huang et al. 2019), their dark matter haloes properties (Gonzalez-Perez et al. 2018; Guo et al. 2019; Gonzalez-Perez et al. 2020), and alternative methods to improve the removal of systematics in their clustering (Kong et al. 2020; Rezaie et al. 2020).

This paper is part of a series of papers presenting the final DR16 data and cosmological results. The LRG and QSO LSS catalogues are presented in Ross et al. (2020); the QSOs LSS catalogues use the DR16 QSO catalogues presented in Lyke et al. (2020). The *N*-body mocks, along with mock challenges done to validate the eBOSS analysis, are presented in Rossi et al. (2020, LRGs), Alam et al. (2020); Avila et al. (2020, ELGs), and Smith et al. (2020, QSOs). The approximate mocks are presented in Zhao et al. (2020a, EZmocks) and Lin et al. (2020, QPM-GLAM). The anisotropic clustering analyses are presented in configuration space in Bautista et al. (2020, LRGs), Tamone et al. (2020, ELGs), Wang et al. (2020, ELGs and LRGs), Hou et al. (2020, QSOs), and in Fourier space in Gil-Marín et al. (2020, LRGs), de Mattia et al. (2020, ELGs), Zhao et al. (2020b, ELGs and LRGs), and Neveux et al. (2020, QSOs). The Ly α auto- and cross-correlations are presented in des Mas du Bourboux et al. (2020). Lastly, the cosmological implication of the full eBOSS sample is presented in eBOSS Collaboration (2020). A summary of all SDSS BAO and RSD measurements with accompanying legacy figures, along with the full cosmological interpretation of these measurements, is available online.[4]

The paper is organized as follows. Section 2 briefly summarizes the target selection and presents the spectroscopic observations and the $z_{\rm spec}$ measurement. The building of the LSS catalogues is detailed in Section 3, including the random catalogue construction, the angular veto masking, and the definition of the weights to correct for non-cosmological fluctuations in the data. The mock catalogues used for the spherically averaged BAO analysis are introduced in Section 4, and the spherically averaged BAO analysis in configuration space is presented in Section 5. We conclude in Section 6.

2 DATA

We describe in this section the target selection, the spectroscopic observations, and the spectroscopic redshift ($z_{\rm spec}$) estimation of the eBOSS/ELG sample.

2.1 Imaging and target selection

The ELG target selection is extensively described in Raichoor et al. (2017) to which we refer the reader for more details.

Targets are selected using the DECaLS part of the Legacy Imaging Surveys[5] (Dey et al. 2019) *grz* photometry, which also provides the imaging for the DESI target selection. In detail, the DECaLS program is a consistent processing of public imaging taken with the Dark Energy Camera (DECam Flaugher et al. 2015), mostly coming from the DECaLS survey (co-PIs: A. Dey and D.J. Schlegel; NOAO Proposal # 2014B-0404) and the DES[6] (PI: J. Frieman; NOAO Proposal # 2012B-0001). Comparat et al. (2016) and Raichoor et al. (2016) demonstrated that DECaLS permits a better target selection in terms of higher redshift and density than the SDSS imaging. The footprint is divided in two parts (see Fig. 1): $\sim$620 deg^2 in the Fat Stripe 82 in the South Galactic Cap (SGC) at -43°<R.A.<45° and -5°<Dec.<5°, covered by the DES and $\sim$550 deg^2 in the North Galactic Cap (NGC) at 126°<R.A.<166° and 13.8°<Dec.<32.5°, covered by the DECaLS survey. The DES imaging we use in the SGC is $\sim$0.5 mag deeper than the DECaLS imaging used in the NGC.

The target selection is based on the catalogues produced by the Legacy Imaging Surveys software, `legacypipe`,[7] which uses the `Tractor` (Lang, Hogg & Mykytyn 2016) library for source measurement. The `legacypipe` analysis splits the sky into *bricks* ($0.25^\circ \times 0.25^\circ$) and outputs products at the brick level. The DECaLS/DR3 version was used, except for part of the NGC footprint (chunk `eboss25`), which was performed later: as the DECaLS/DR3 pipeline could not be run anymore because of a major PYTHON update done on all the machines, the target selection was performed on catalogues created by the DECaLS/DR5 pipeline. We used a slightly edited version of DECaLS/DR5 `Tractor`, using PS1 for astrometric calibration and relaxing the CCD quality cut, to prevent holes in the footprint.[8] Tests on a few square degrees having the exact same exposures between DECaLS/DR3 and DECaLS/DR5 showed that $\sim$15 per cent of the targets differ between the two pipeline versions. Differences are on the faint *g*-band magnitude side of the selection, with no specific behaviour, and hence are consistent with scatter across the faint end cut.

The target selection, detailed in table 2 of Raichoor et al. (2017), consists of: (i) a cut in the *g*-band magnitude to select [O II] emitters; (ii) a box selection in the *grz*-diagram, with a smaller box in the NGC to prevent contamination from low-redshift objects due to shallower imaging; and (iii) a clean photometry criterion (combination of cuts on `legacypipe` output columns and of some geometrical masks). All magnitudes are corrected for Galactic extinction with maps from Schlegel, Finkbeiner and Davis (1998). We report here the magnitude

[1]Prime Focus Spectrograph: http://sumire.ipmu.jp/en/2652/
[2]Dark Energy Spectroscopic Instrument: http://desi.lbl.gov/cdr/
[3]Wide-Field Infrared Survey Telescope: https://wfirst.gsfc.nasa.gov/
[4]https://www.sdss.org/science/final-bao-and-rsd-measurements/, https://www.sdss.org/science/cosmology-results-from-eboss/
[5]http://legacysurvey.org/
[6]http://www.darkenergysurvey.org
[7]https://github.com/legacysurvey/legacypipe
[8]https://github.com/legacysurvey/legacypipe/tree/dr5.eboss, https://github.com/legacysurvey/legacypipe/tree/dr5.eboss2

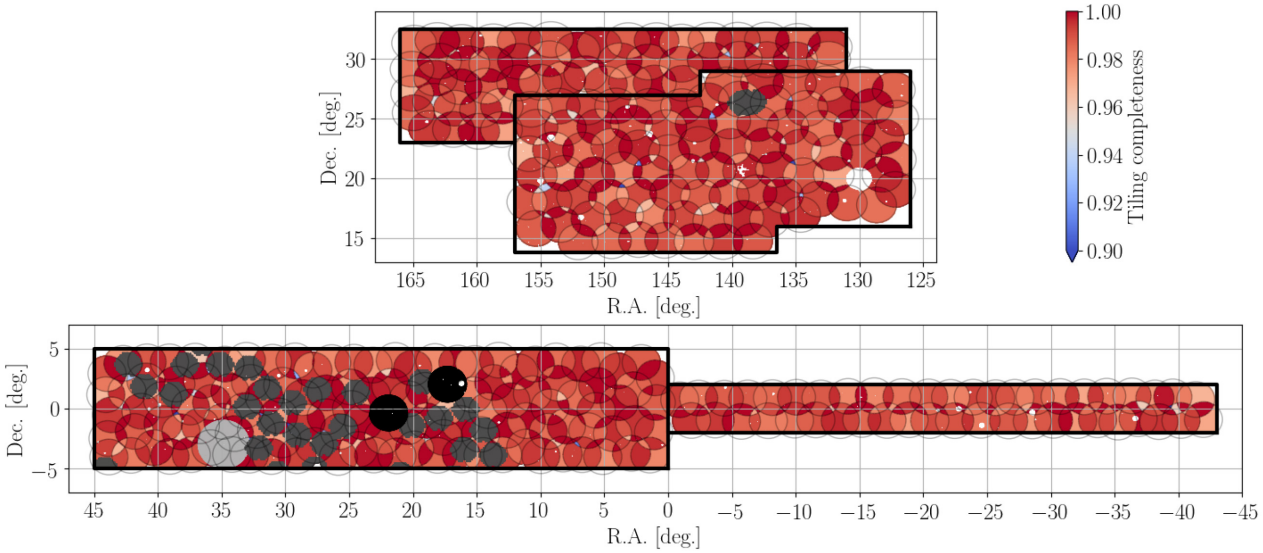

Figure 1. Geometry of the ELG program. The NGC tiling is presented in the top panel: chunk `eboss23` is at lower Dec. and chunk `eboss25` at higher Dec. The SGC tiling is presented in the bottom panel: chunk `eboss21` is at R.A.$<0°$ and chunk `eboss22` at R.A.$>0°$. The colour-coding is the tiling completeness (COMP_BOSS), which represents the fraction of resolved fibres per sector (see Section 3.4). Additionally, we overlay some a posteriori angular veto masks, which are detailed in Section 3.2: Mira star (light grey), DECam pointings with bad photometric calibration (dark grey), and two low-quality spectroscopic plates (black). The regions without targets at R.A$\sim$130° and Dec.$\sim$20° correspond to the open cluster NGC 2632.

cuts for SGC:

$$21.825 < g < 22.825 \tag{1a}$$

$$-0.068 \times (r-z) + 0.457 < g - r < 0.112 \times (r-z) + 0.773 \tag{1b}$$

$$0.218 \times (g-r) + 0.571 < r - z < -0.555 \times (g-r) + 1.901 \tag{1c}$$

and here the magnitude cuts for the NGC:

$$21.825 < g < 22.9 \tag{2a}$$

$$-0.068 \times (r-z) + 0.457 < g - r < 0.112 \times (r-z) + 0.773 \tag{2b}$$

$$0.637 \times (g-r) + 0.399 < r - z < -0.555 \times (g-r) + 1.901. \tag{2c}$$

It provides a list of 269 718 targets.

2.2 Spectroscopic observations

The ELG spectroscopic observations are conducted with the BOSS spectrograph (Smee et al. 2013) at the 2.5-m aperture Sloan Foundation Telescope at Apache Point Observatory in New Mexico (Gunn et al. 2006). The BOSS spectrographs resolution for 5950 Å$< \lambda <$ 7850 Å, where the [O II] doublet lies for $0.6 < z < 1.1$, is $1800 < R < 2500$, which does not permit to clearly resolve the [O II] doublet (Comparat et al. 2013). 1000 objects are observed at once, with 1000 fibres plugged into a drilled plate, among which $\sim$850 are assigned to ELGs. 305 plates have been allocated to the ELG program and observations were undertaken between September 2016 and February 2018 ($57656 \leq$ `MJD` ≤ 58171). Targeting was performed on subsets of the full eBOSS/ELG area, called chunks: the SGC is divided in two chunks, `eboss21` and `eboss22`, and the NGC is divided in two chunks, `eboss23` and `eboss25`. Observations are designed by defining the plate tiling (Blanton et al. 2003), which optimizes for each chunk the fraction of targets having a fibre for the budgeted number of plates. Fig. 1 shows the plate tiling, with the tiling completeness, defined as the fraction of resolved targets (see Section 3.4, this corresponds to the COMP_BOSS quantity in previous BOSS/eBOSS analysis). We note the narrow width (4°) of the `eboss21` chunk in the Dec. direction, which is constrained by the available imaging. Given it is the order of the size of the BAO scale, this is likely not an optimal geometry, but it is not a significant problem as the R.A. and radial directions provide numerous ELG pairs at the BAO scale. Besides, this is fully accounted for in our analysis with our random catalogues (Section 3) and with the validation of the analysis with the mock catalogues (see Sections 4 and 5). We report in Table 1 the details of the spectroscopic observations for each chunk and for the whole programme.

Details of the spectroscopic setup are presented in Raichoor et al. (2017). Each plate is observed with individual exposures of 15 min until $\texttt{rSN}^2 > 22$, where $\texttt{rSN}^2$ is the median-squared signal-to-noise ratio (SN) in the red camera evaluated at the mountain. This is reached on average with 4.7 × 15 min exposures; the average SN on individual ELG spectra[9] is $\sim$0.8. During the first month of operations (around half of the `eboss21` chunk), observations were done with higher $\texttt{rSN}^2$ ($\sim$40).

If one plate has to be unplugged before it reaches the minimum $\texttt{rSN}^2$, it is plugged again later and re-observed: as the fibres are not assigned to the same targets between the two pluggings, this results in two PLATE-MJD reductions for the considered plate. This provides valuable independent, repeat observations for ELGs on that plate, which allows us to quantify the reliability of our redshift measurement (see Section 2.3).

[9]i.e. the average value of the `idlspec2d` `SN_MEDIAN_ALL` quantity, which measures the median signal to noise per pixel across full spectrum in physical units of erg.s^{-1}.cm^{-2}.Å^{-1}; see column (8) of Table 1.

Table 1. Spectroscopic observations properties per chunk: (1): chunk name; (2): tiling area (deg^2); (3): number of plates; (4): number of PLATE-MJD reductions; (5): average observed time in minutes per PLATE-MJD; (6): average observed time in minutes included in the reduction per PLATE-MJD; (7): mean plate rSN^2; (8): mean SN per spectrum; (9): number of targets; (10): number of observed spectra; (11): number of spectra after removing duplicates; (12): number of targets after applying the veto LSS masks; (13): number of star spectra after applying the veto LSS masks; (14): number of galaxy spectra after applying the veto LSS masks; and (15): number of galaxy spectra after applying the veto LSS masks and with a reliable redshift.

(1) Chunk	(2) Area (deg^2)	(3) $N_{\rm PLATE}$	(4) $N_{\rm PLATE}^{\rm MJD}$	(5) $t_{\rm exp}^{\rm obs}$ (min)	(6) $t_{\rm exp}^{\rm kept}$ (min)	(7) rSN^2	(8) SN$_{\rm spec}$	(9) $N_{\rm targ}$	(10) $N_{\rm spec}^{\rm obs}$	(11) $N_{\rm spec}^{\rm obs,uniq}$	(12) $N_{\rm targ}^{\rm LSS}$	(13) $N_{\rm spec}^{\rm LSS,star}$	(14) $N_{\rm spec}^{\rm LSS,gal}$	(15) $N_{\rm spec,reliable}^{\rm LSS,gal}$
eboss21	171	46	46	122	100	28.7	0.99	40904	38992	38493	36314	333	33884	31200
eboss22	445	121	131	86	73	22.1	0.85	106897	111061	101954	79880	512	75585	69071
eboss23	377	87	92	70	60	25.4	0.82	76236	76250	71134	70935	544	65677	58648
eboss25	178	51	51	59	54	24.6	0.81	45141	42940	42863	42565	315	40141	36166
all	1170	305	320	82	70	24.0	0.84	269178	269243	254444	229694	1704	215287	195085

Because of dead fibres or observational issues (e.g. incorrect plugging of a fibre), some spectra are unusable. We identify those cases by using the ZWARNING quantity output by the redshift fitter (see table 3 of Bolton et al. 2012): when one of the LITTLE_COVERAGE, UNPLUGGED, BAD_TARGET, or NODATA bits is turned on, we label the fibre as not valid, and as a consequence, we discard the spectrum and consider that no spectroscopic observation has been taken.

Overall, there are 14 799 repeat ELG spectra, or duplicates. Duplicates happen for two reasons. First, when a PLATE has several MJD reductions: all ELGs on the plate will have as many $z_{\rm spec}$ measurements as MJD reductions. In that case, we consider as primary spectra all spectra coming from the MJD reduction with the higher plate SN, and as duplicates, the spectra from the other MJD reductions. Secondly, in the plate overlap regions, any remaining fibres are assigned to repeats: the fibre is then assigned to a target, which already has a fibre assigned from another overlapping plate. In that case, we consider as primary the spectrum with a valid fibre and with the highest χ^2 difference between the best-fitting solution and the second best-fitting solution.

2.3 Spectroscopic redshift estimation: `redrock`

The results presented in this paper use version v5_13_0 of the idlspec2d data reduction pipeline to extract and flux-calibrate the ELG 1D spectra from the raw 2D spectroscopic images (Bolton et al. 2012; Ahumada et al. 2020). As stated in Raichoor et al. (2017), the BOSS/eBOSS redshift fitter, idlspec1d, is not optimized for ELGs, as it has been designed for bright LRGs. Therefore, we used for the 1D spectrum analysis redrock,[10] the DESI redshift fitter, which provides more reliable redshifts.

We present here a summary of the redrock principle; we refer the reader to Ross et al. (2020) for more details. redrock templates, labelled archetypes, are the most representative (simulated) physical spectra of DESI galaxies, QSOs, and stars. redrock fitting procedure includes two steps. In the first step, it finds the χ^2 minima using principal-component analysis (PCA) templates, based on DESI archetypes. As the best-fitting PCA spectra can be non-physical, for each minimum vicinity, redrock then recomputes the χ^2 with archetypes. This approach ensures that the best-fitting solution corresponds to a physical, meaningful, spectrum.

Following the eBOSS requirements (Dawson et al. 2016; Raichoor et al. 2017), redshift estimates should be precise ($|\Delta v| < 300$ km s^{-1}) and accurate (less than 1 per cent catastrophic redshifts, defined as $|\Delta v| > 1000$ km s^{-1}). To match these requirements, we define a redshift estimate reliable if the following criteria are satisfied:

(ZWARNING == 0) and (3a)

(SN_MEDIAN[i] > 0.5 or SN_MEDIAN[z] > 0.5) and (3b)

(zQ >= 1 or zCont >= 2.5). (3c)

In the following, we call a 'failure' a redshift measurement that does not pass those equations, i.e. which is not considered as reliable. The first criterion (equation 3a) is based on the ZWARNING flag output by redrock (see Section 2.2) and ensures that the fitting did not encounter any problems. In particular, it assures that the coefficient in front of the best-fitting archetype spectrum is positive, meaning that the best-fitting template is physically motivated (see Ross et al. 2020). The second criterion (equation 3b) ensures a minimum SN in the red part of the spectrum, where the [O II] line is expected to be observed at $z \sim 1$.[11] The third criterion (equation 3c) reduces the fraction of catastrophic redshifts; it is based on the {zQ, zCont} a posteriori flags (see Comparat et al. 2016; Raichoor et al. 2017), which quantify the emission lines and continuum level of information. The impact of each cut, along with the improvement with respect to idlspec1d, is shown in Table 2 (the catastrophic rate is estimated with repeat observations, as described further in this section). One can see the significant improvement brought by redrock with respect to the reliability criterion presented in Raichoor et al. (2017), based on idlspec1d: it allows us to include in our cosmological $0.6 < z_{\rm spec} < 1.1$ sample more reliable redshifts (80.7 per cent versus 74.0 per cent, for a Poissonian fluctuation of ∼0.3 per cent), with a lower fraction of catastrophic rate (0.3 per cent versus 0.5 per cent, for a Poissonian fluctuation of ∼0.06 per cent). Those improvements are significant, well above the Poissonian noise fluctuations. We validate our reliability criteria with two approaches, visual inspection and repeat observations.

Three plates have been visually inspected, one from the eBOSS/ELG program (PLATE-MJD = 9236-57685) and two from pilot ELG programs (PLATE-MJD = 6931-56388 and 8123-56931). We restrict here to the ∼1900 ELGs with $0.6 < z_{\rm spec} < 1.1$ that passed our reliable criteria listed in equations (3a), (3b), and (3c). The inspector assigns a visual redshift and one of the following

[10] https://github.com/desihub/redrock; we used a customed version of the tagged version 0.14.0, where we do not use the ANDMASK masking, as it unnecessarily removes pixels close to sky emission lines from the fit, hence creating artificial drops in the redshift density n(z), where the [O II] doublet falls close to sky lines; that version is internally labelled v5_13_0_no_andmask.

[11] SN_MEDIAN[i,z] is the median SN for all good pixels from the spectrum corresponding to the i- and z-bands.

Table 2. Reliable redshift statistics for various criteria. We use the last line criterion. Estimate from our catastrophic rates is computed from repeat observations; see Table 3 for our visual inspection results.

Redshift fitter	Criterion	Reliable z_{spec}	Reliable $0.6 < z_{spec} < 1.1$	Catastrophic z_{spec}	Catastrophic $0.6 < z_{spec} < 1.1$
`idlspec1d`	Equation (1) of Raichoor et al. (2017)	83.1%	74.0%	0.5%	0.5%
`redrock`	Equation (3a)	93.0%	82.0%	0.7%	0.6%
`redrock`	Equation (3a) and equation (3b)	91.8%	81.3%	0.6%	0.6%
`redrock`	Equation (3a), equation (3b), and equation (3c)	90.6%	80.7%	0.3%	0.3%

Table 3. Redshift measurement assessment from visual inspection of three plates for ∼1900 ELGs, with $0.6 < z_{spec} < 1.1$ and passing equations (3a), (3b), and (3c). The visual inspection confidence flag meaning is: 3: definitely correct, 2: features are visible and the redshift is likely to be correct, 1: information in the spectrum, but the redshift is a guess, and 0: no information, useless spectrum. For instance, 24.0 per cent of the inspected spectra have confidence = 2, and 99.3 per cent of those have $|\Delta v| < 300$ km s^{-1}.

Conf. Flag	Percentage	$\lvert\Delta v\rvert < 300$ km s^{-1}	$\lvert\Delta v\rvert < 1000$ km s^{-1}
3	71.5%	99.9%	99.9%
2	24.0%	99.3%	99.6%
1	2.9%	94.5%	96.3%
0	1.6%	6.5%	6.5%
All	100%	98.1%	98.2%

confidence flags: 3: definitely correct, 2: features are visible and the redshift is likely to be correct, 1: information in the spectrum, but the redshift is a guess, and 0: no information, useless spectrum. Visual inspection results are reported in Table 3. The `redrock` redshift is almost in perfect agreement (99.8 per cent with $|\Delta v| < 300$ km.s^{-1}) with the inspector redshift for confidence = 3 and confidence = 2 (95.5 per cent of the sample). For confidence = 1 (2.9 per cent of the sample), both redshift estimations mostly agree (∼95 per cent). For confidence = 0 (1.6 per cent of the sample), we can conservatively assume that the pipeline is wrong in most cases. Overall, based on these visual inspections, we estimate that the pipeline provides a redshift precision better than 300 km s^{-1} for 98.1 per cent of our sample and a catastrophic redshift for ∼1.8 per cent of our sample.

We present a second, independent estimate of catastrophic rate with repeat observations, which provides us with ∼17 000 pairs of observations of a given target. We restrict to the ∼13 000 repeats where both redshift estimations pass our reliability criterion and consider a pair is catastrophic if the two redshift measurements differ by more than 1000 km s^{-1}. Following this approach, we find that 0.3 per cent of the sample have a catastrophic redshift measurement. Additionally, we can assess with repeats that 99.5, 95, and 50 per cent of our redshift estimates have a precision better than 300 km s^{-1}, 100 km s^{-1}, and 20 km s^{-1}, respectively.

Lastly, we assess our redshift measurements with comparing with two external datasets overlapping our eBOSS/ELG footprint: DEEP2 (Newman et al. 2013), which observations were done with the DEIMOS spectrograph (resolution $R \sim 5900$) on the Keck II 10-m telescope, and WiggleZ (Drinkwater et al. 2010), which observations were done with the AAOmega spectrograph (resolution $R \sim 1300$) on the AAT 3.9-m telescope. When restricting on our eBOSS/ELG sample with a reliable redshift within 0.6 and 1.1, we find 146 matches with DEEP2 objects having a reliable redshift ($Q = 4, 5$) and 216 matches with WiggleZ objects having a reliable redshift ($Q = 4, 5$). Our eBOSS/ELG measurements are in good agreement with the DEEP2 and WiggleZ ones: for DEEP2 (WiggleZ), we measure a mean difference of $\Delta v = 16 \pm 39$ km s^{-1}(-2 ± 47 km s^{-1}) and only 1/146 (2/216) objects have $\Delta v > 1000$ km s^{-1}.

We thus conclude that the `redrock` redshift measurements passing our equations (3) are precise (precision better than 300 km s^{-1} for ∼99 per cent of our sample) and accurate (expected catastrophic rate of ∼1 per cent), thus fulfilling the eBOSS/ELG requirements set at the beginning of the program.

Table 4. Statistic for the ELG sample. The reported N are computed after applying the LSS veto masks. A target is either observed or unobserved because of close pairs or lack of fibre: $N_{obs} + N_{cp} + N_{miss} = N_{targ}$. Similarly, an observed target is classified as a star, as a galaxy, or a redshift failure (i.e. does not pass equations 3): $N_{star} + N_{gal} + N_{zfail} = N_{obs}$. N_{used} is the number of galaxies with $0.6 < z_{spec} < 1.1$. The geometric area is the tiling area, i.e. covered by the plates. The unvetoed area is the area after applying the LSS veto masks. The effective area is the unvetoed area after accounting for the tiling completeness.

	NGC	SGC	Total
N_{targ}	113 500	116 194	229 694
N_{obs}	106 677	110 314	216 991
N_{cp}	5805	4797	10 602
N_{miss}	1018	1083	2 101
N_{gal}	94 814	100 271	195 085
N_{star}	859	845	1704
N_{zfail}	11 004	9198	20 202
N_{used}	83 769	89 967	173 736
Geometric area (deg^2)	554.1	616.1	1170.2
Unvetoed area (deg^2)	372.8	360.9	733.8
Effective area (deg^2)	369.5	357.5	727.0
Effective volume (Gpc^3)	0.30	0.30	0.60

3 LARGE-SCALE STRUCTURE CATALOGUES CREATION

We detail in this section the building of the LSS catalogues. These LSS catalogues are used in this paper to measure the spherically averaged BAO in configuration space. They are also used in de Mattia et al. (2020) and Tamone et al. (2020) for the measurement of the growth rate of structures and BAO in Fourier space and in configuration space, respectively. They are publicly available.[12]

Table 4 summarizes the overall properties of these LSS catalogues. The steps to build the LSS catalogues are: (1) define starting data and random samples; (2) define and apply the angular veto masks to the data and the randoms; (3) define weights to correct for non-cosmological fluctuations (redshift failures: w_{noz}, close pairs: w_{cp}, systematics due to photometry: w_{sys}), and optimize the contribution

[12]A link to web page will be provided after DR16 papers are accepted for publication.

Table 5. Angular veto mask properties. Bits 1, 2, 3, 4, and 5 have been applied before the target selection (the few removed targets are due to slightly different implementation). Apart from the `eboss22` two low-quality plates removal, all veto masks are bit-coded (in the mskbit column in the catalogues).

Bit	Mask	Removed area (deg^2)	Removed targets
1	Not g+r+z	67.2	27
2	xybug	49.7	0
3	Recovered `decam_anymask`	210.1	142
4	`tycho2inblob`	4.7	0
5	Bright objects	57.6	7
6	*Gaia* stars	54.0	17 456
7	Mira star	12.5	3555
8	Imprecise mskbit 3	0.1	15
9	centerpost	0.6	166
10	TDSS_FES targets	1.3	308
11	DECam bad phot. calib.	72.7	16 325
–	`eboss22` low-quality plates	13.9	3123
–	Total	436.5	41 124

of galaxies based on their number density at different redshifts and apply inverse-variance weights $w_{\rm FKP}$; and (4) assign redshifts to the randoms.

3.1 Data selection, random catalogues

To construct the LSS catalogues, we first remove duplicates and restrict to ELGs with a valid fibre and a reliable $z_{\rm spec}$ estimate with $0.6 < z_{\rm spec} < 1.1$: this provides 173 736 unique ELGs.

We generate random catalogues (randoms), which will have the same angular and radial distribution as the ELG data. We first create random angular positions at a constant angular density of 10^4 deg^{-2}, i.e. $\sim$40$\times$ the ELG target density, over the full sky. We then remove any random outside of any chunk.

3.2 Angular veto masks

In addition to the geometry of the plate tiling, we apply several angular veto masks to our LSS data and random catalogues where, for various reasons, we could not reliably observe galaxies. Table 5 lists all those angular veto masks, along with the masked area and the number of masked targets.

Masks corresponding to bit values 1–5 in Table 5 were applied at the target selection level, before the tiling (those are described in Raichoor et al. 2017). The other masks are applied in the analysis step, after the spectroscopic observations: those additional angular masks remove a significant number of targets but are necessary to provide a clean, reliable LSS catalogue.

Masks corresponding to bit values 1 through 4 rely on the photometric `legacypipe` pipeline outputs, stored (or recovered for bit = 3) at the brick level. Those outputs are the photometric catalogues but also various brick-sized images (3600 × 3600 pixels, with 0.262 arcsec/pixel), such as the depth images. We detail below each veto angular mask.

(i) not g+r+z (bit = 1): the target selection requires that *grz* photometry is available: this de facto excludes regions not covered by *grz* imaging. Those regions can be identified with the `legacypipe` depth images.

(ii) (x,y) bug (bit = 2): as stated in Raichoor et al. (2017), a bug at the target selection level resulted in an additional angular masking. This affects the `eboss23` chunk but also – to a lesser extent – the `eboss21` and `eboss22` chunks; the `eboss25` chunk is not affected by this mask. This mask can be exactly recovered with using the `legacypipe` depth images.

(iii) `decam_anymask` (bit = 3): in the target selection, we required `decam_anymask [grz]` = 0, where `decam_anymask` is a `legacypipe` quantity, flagging objects where one of the underlying DECam images is defective at the pixel position corresponding to the centre of the object; this flag is often turned on for pixels close to individual imaging CCD edges along the R.A.. In the DECaLS/DR3 version, the `decam_anymask` information is stored only where objects are detected, making it extremely difficult to propagate that information to the random sample; however, since the DECaLS/DR7 version, this information is stored at the pixel level for each brick, making it recoverable at any location. We thus re-run the part of the DECaLS/DR7 pipeline on the exact DECam imaging data set used for the ELG target selection (smaller than the DECaLS/DR7 one) to produce that output, having in this way the `decam_anymask` information at the pixel level.

(iv) `tycho2inblob` (bit = 4): in the target selection, we required `tycho2inblob = False`, where `tycho2inblob` is a `legacypipe` column flagging objects whose light profile overlaps one of the Tycho2 stars (Høg et al. 2000). The `legacypipe` pipeline stores for each brick that information.

(v) bright objects and Tycho2 stars (bit = 5): we used geometrical masks to veto the surrounding area of SDSS bright objects[13]; we also define a circular mask for each 0 mag $< V <$11.5 mag Tycho2 star with radius = $10^{3.5\,-\,0.15\,\times\,V}$ arcsec, where V is the Tycho2 star `MAG_VT` quantity from Høg et al. (2000).

(vi) *Gaia* stars (bit = 6): The *Gaia*/DR2 release (Gaia Collaboration 2018) allows one to select a clean star sample for $12 < G < 17$, where it is complete,[14] hence nicely completing the Tycho2 star sample. After defining a criterion to identify stars,[15] we group the selected stars in one magnitude bin and, for each bin, analyse the ELG target density and the SSR (Spectroscopic Success Rate defined in equation 4) as a function of the distance to the stars. We observe that, close to *Gaia* stars, we select more targets, have more failures, and the redshift distribution is different: it is very likely that the excess targets correspond to artefacts in the DECaLS imaging or real objects with unreliable photometry, hence increasing the target density and the failure rate, and changing the redshift distribution. We define a circular mask for each *Gaia* star with $0 < G < 16$ with radius = $10^{2.32\,-\,0.07\,\times\,G}$ arcsec, chosen by analysing the variations of the target density, the redshift failure rate, and the redshift distribution.

(vii) Mira star (bit = 7): The Mira star (R.A = 34.84°, Dec. = −2.98°) is a well-known variable star, with a variability amplitude of several magnitudes. As a consequence, its magnitude in the Tycho2 catalogue is not representative of its magnitude during the DECam observations. We conservatively use a circular mask with a 2° radius around the Mira star. This mask is displayed in light grey in Fig. 1.

(viii) imprecise recovered `decam_anymask` (bit = 8): our approach to recover the `decam_anymask` value at each position of the sky to apply the bit = 3 masking does not perfectly match the DECaLS catalogues used for target selection, i.e. it does not perfectly reproduce what has been used at the target selection level. We account

[13] https://data.sdss.org/sas/dr10/boss/lss/reject_mask/

[14] https://www.cosmos.esa.int/web/gaia/dr2

[15] If we note gmag and excess the `PHOT_G_MEAN_MAG` and `astrometric_excess_noise` quantities, our criterion is: excess = 0 or $\log_{10}$(excess)<0.3 · gmag-5.3 or $\log_{10}$(excess)<-0.5 · gmag+9.0.

for this issue as follows. We use the `Healpix`[16] scheme (Górski et al. 2005) to divide the sky into equal-area small pixels of ∼11 arcmin^2 (corresponding to nside = 1024). We reject 37 pixels where the percentage of objects with an improper recovered `decam_anymask` is greater than 10 per cent.

(ix) centerpost (bit = 9): each plate has a hole in its centre to fix it with the centrepost; as a consequence, no fibre can be placed within 92 arcsec of the plate centre. Contrary to other BOSS/eBOSS targets, the higher ELG density making the tiling denser, this does not result in a 'simple' veto mask, as the position of plate centre can be covered by another adjacent plate (see Fig. 1). However, for simplicity, we simply mask these centerpost regions.

(x) TDSS FES targets (bit = 10): on each ELG plate, ∼50 fibres are assigned to the Time Domain Spectroscopic Survey (TDSS, Morganson et al. 2015; Ruan et al. 2016). A subsample of the TDSS targets, the FES class targets (∼1 deg^{-2}), has been tiled with the same priority as the ELG targets. To account for that, we create around each TDSS FES target a circular veto mask with a radius of 62 arcsec, corresponding to the size of one fibre.

(xi) DECam bad photometric calibration (bit = 11): at the time of DECaLS/DR3, the DECaLS pipeline was including all public *grz*-band DECam imaging over the DECaLS footprint, hence imaging from various different programs. The latest DECaLS/DR8 release[17] mostly restricts to DES and DECaLS observations and has a significantly improved photometric calibration procedure. We take advantage of that data set to verify the photometric calibration of our DECaLS/DR3 and DR5 imaging used for target selection. We identify in this way some observing programs with improper photometric calibration (of the order of tens of mmag): such systematic offset in the photometry implies a different target selection, as it is equivalent to move the boundaries of the photometric cuts. We remove the regions covered by the DECam CCDs belonging to those identified observing programs. This mask is displayed in dark grey in Fig. 1.

(xii) `eboss22` low-quality plates: lastly, we also remove the regions covered by two `eboss22` spectroscopic plates (PLATE-MJD = 9430-58112 and 9395-58113), which have significantly lower-than-average quality. Those plates bias the SSR = f(pSN) fit in equation (6) (see next section). This mask is displayed in black in Fig. 1.

Fig. 2 illustrates the DECaLS-related, bright objects and stars masks for a given DECaLS brick.

We provide in the associated data release the required information to reproduce the angular masking when considering any (R.A., Dec.) position: bits 1–7 can compute with the `brickmask`[18] script, bits 8–11 and the two `eboss22` low-quality plates can be reproduced with customed PYTHON lines.

3.3 Spectroscopic redshift failures

The principle of using ELGs for LSS clustering relies on the fact that it is possible to measure the $z_{\rm spec}$ thanks to emission lines, with no requirement of high SN detection of the continuum, making them an interesting tracer. However, for low SN spectra (see Table 1), the BOSS spectrograph resolution of ∼2000 does not allow the [O II] doublet to be resolved (Comparat et al. 2013), on which

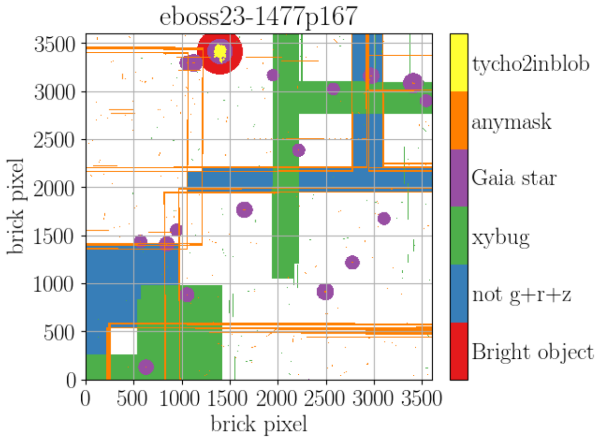

Figure 2. Illustration of the DECaLS-related, bright objects and stars masks for a given DECaLS brick (0.25° × 0.25°, 3600 × 3600 pixels, with 0.262 arcsec/pixel). The xybug mask is the symmetric along the brick diagonal of the not g+r+z mask. The `decam_anymask` mask mostly follows the CCD edges along R.A. (horizontal in the figure).

many $z_{\rm spec}$ measurements rely. As a consequence, redshift failures are significant (∼10 per cent of the observations) and present strong dependencies on observing conditions, which need to be carefully modelled and corrected for in the LSS analysis (see, for instance, Blake et al. 2010; Bautista et al. 2018; Addison et al. 2019).

We define the SSR as:

$$\mathrm{SSR} = \frac{N_{\rm gal}}{N_{\rm gal} + N_{\rm zfail}}, \tag{4}$$

where $N_{\rm gal}$ is the number of spectra with a valid fibre, a reliable $z_{\rm spec}$ estimate, and not being a star, and $N_{\rm zfail}$ is the number of spectra with a valid fibre but no reliable $z_{\rm spec}$ estimate and not a star. We beforehand apply all angular veto masks described in Section 3.2.

To correct redshift failures, we derive weights from a fit of the SSR as a function of two quantities, which correlate with the angular position of the fibres on the sky, namely the plate-average SN (pSN[19]) and the (XFOCAL, YFOCAL) position in the focal plane:

$$w_{\rm noz} = \frac{1}{f_{\rm noz,pSN} \cdot f_{\rm noz,XYFOCAL}}, \tag{5}$$

We perform the fit for each half-spectrograph (Spectro_1a: 1 ≤ `FIBERID` ≤ 250, Spectro_1b: 251 ≤ `FIBERID` ≤ 500, Spectro_2a: 501 ≤ `FIBERID` ≤ 750, Spectro_2b: 751 ≤ `FIBERID` ≤ 1000) of each chunk (`eboss21`,`eboss22`, `eboss23`, `eboss25`). The rationale behind this approach stems from the specificity of each chunk and the different response of each half-spectrograph. Indeed, `eboss21` has longer spectroscopic exposure time on average and a particular geometry (hence having a non-standard position of the fibres in the focal plane), `eboss21` and `eboss22` have DES, deeper imaging, while `eboss23` imaging is shallower and `eboss25` imaging comes from a different DECaLS release. It is known that the second spectrograph (501 ≤ `FIBERID` ≤ 1000) has a better throughput (Smee et al. 2013): we do observe differences due to this for our ELG sample, and we also observe that half-spectrographs have different responses; for instance, the mean SN per spectra is 0.91, 0.87, 0.94, 0.88 for Spectro_1a, Spectro_1b, Spectro_2a, Spectro_2b, respectively. We currently do not find an explanation for that half-spectrograph difference in the mean SN. For simplicity,

[16] http://healpix.jpl.nasa.gov
[17] http://legacysurvey.org/dr8
[18] https://github.com/cheng-zhao/brickmask/releases/tag/v1.0

[19] i.e. the average `SN_MEDIAN_ALL` for the ELG spectra.

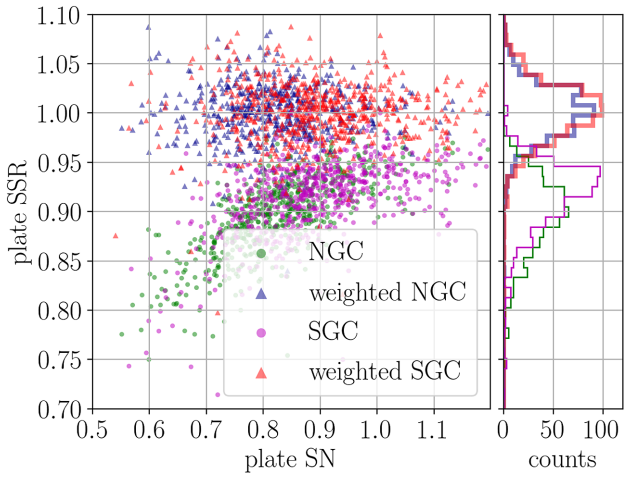

Figure 3. Fraction of reliable z_{spec} (SSR) per plate, as a function of the plate SN: each dot represents a PLATE-MJD reduction. For the NGC/SGC, the SSR before weighting by $1/f_{noz,pSN}$ is displayed in green/magenta dots and the SSR after weighting by $1/f_{noz,pSN}$ is displayed in blue/red triangles. The model is fitted to each half-spectrograph for each chunk.

we display in Figs 3–5 the fitted results for all fibres from each Galactic cap.

The first quantity is the overall SN of the plate, pSN. As observations are performed at a rather low SN, the fraction of redshift failures increases quickly for lower-than-average observing conditions. In Fig. 3, we display the plate SSR, i.e. the fraction of reliable z_{spec} per plate, as a function of the plate SN. We model the SSR dependence on the plate SN with the following function:

$$f_{noz,pSN}(x) = c_0 - c_1 \times |x - c_2|^{c_3}, \quad (6)$$

where x is the pSN and the four coefficients c_0, c_1, c_2, and c_3 are fitted through a χ^2 minimization. For each fit, the number of fitted points is the number of plates per chunk, reported in column (3) of Table 1. Fig. 3 illustrates how the data populate the pSN, SSR space, before (dots) and after (triangles) the weighting by $1/f_{noz,pSN}$. Once weighted, the SSR is independent of the plate SN.

The second quantity we use is the (XFOCAL,YFOCAL) position. On average, fibres from Spectro_1a are at YFOCAL<0, XFOCAL>0, from Spectro_1b at YFOCAL<0, XFOCAL<0, from Spectro_2a at YFOCAL>0, XFOCAL<0, and from Spectro_2b at YFOCAL>0, XFOCAL>0. We model the SSR dependence on (XFOCAL,YFOCAL) with the following function:

$$f_{noz,XYFOCAL}(x, y) = c_0 - c_1 \times |x - c_2|^{c_3} - c_4 \times |y - c_5|^{c_6}, \quad (7)$$

where (x, y) are the centre coordinates of bins in the (XFOCAL,YFOCAL) plane, and the seven coefficients c_0, c_1, c_2, c_3, c_4, c_5, and c_6 are fitted through a χ^2 minimization. For each fit, the number of fitted points is ∼350, the number of bins in the (XFOCAL,YFOCAL) plane. Fig. 4 illustrates the behaviour for the NGC (Fig. 5 is similar for the SGC). The top panels show the data before the weighting by $/1f_{noz,\,XYFOCAL}$. Some regions have either systematically lower-than-average (XFOCAL∼−300, YFOCAL∼−100; or extreme XFOCAL values) or higher-than-average (XFOCAL∼−50, YFOCAL∼50) SSR. Our fitted model correctly reproduces that behaviour, as one can see from the red line in the side top panels, or in the bottom panels, which display the SSR after weighting by $1/f_{noz,XYFOCAL}$.

In order to quantify the goodness of the fit for equations (6) and (7), we use the set of 1000 EZmocks with systematics described in

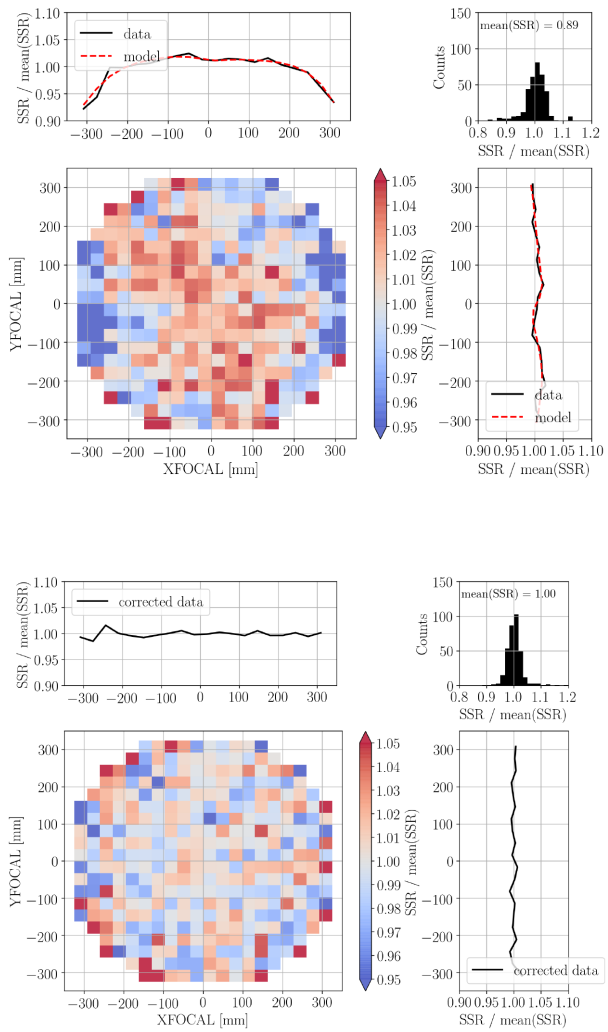

Figure 4. Fraction of reliable z_{spec} (SSR) as a function of XFOCAL and YFOCAL for the NGC, before (top panels) and after (bottom panels) weighting by $1/f_{noz,XYFOCAL}$. The top- and right-side panels show the SSR as a function of XFOCAL and YFOCAL; the top-right histograms display the distribution of the normalized SSR. The model is fitted to each half-spectrograph for each chunk.

Section 4.2. For each fit on the data, i.e. for each half-spectrograph of each chunk, we compare the rms (weighted by the number of objects in each bin) of the SSR after correction by the redshift failure weights, i.e. the weighted rms of the histogram in the right-hand panel of Fig. 3, which we call $\sigma_{w,pSN}$. In the baseline case where redshift failures are injected into the mocks deterministically following their nearest neighbour in the data, virtually all mocks have $\sigma_{w,pSN}$ larger than the data, as expected since the redshift failure implementation departs from the fitted model. Additionally, for each mock, we generate an alternative version where the redshift failures are injected in a stochastic way with a probability following the model predicted SSR of the nearest neighbour in the data. In this case, very few mocks (≃2/1000) have $\sigma_{w,pSN}$ larger than the data. Using the same criterion for the fit performed in bins of (XFOCAL,YFOCAL), we find a slightly better agreement, with ≃20/1000 having a larger $\sigma_{w,XYFOCAL}$. We therefore conclude that the fitted model may be too simple to fully describe the complex systematics of the data. However, comparing cosmological fits performed with the two sets of mocks mentioned above, de Mattia et al. (2020)

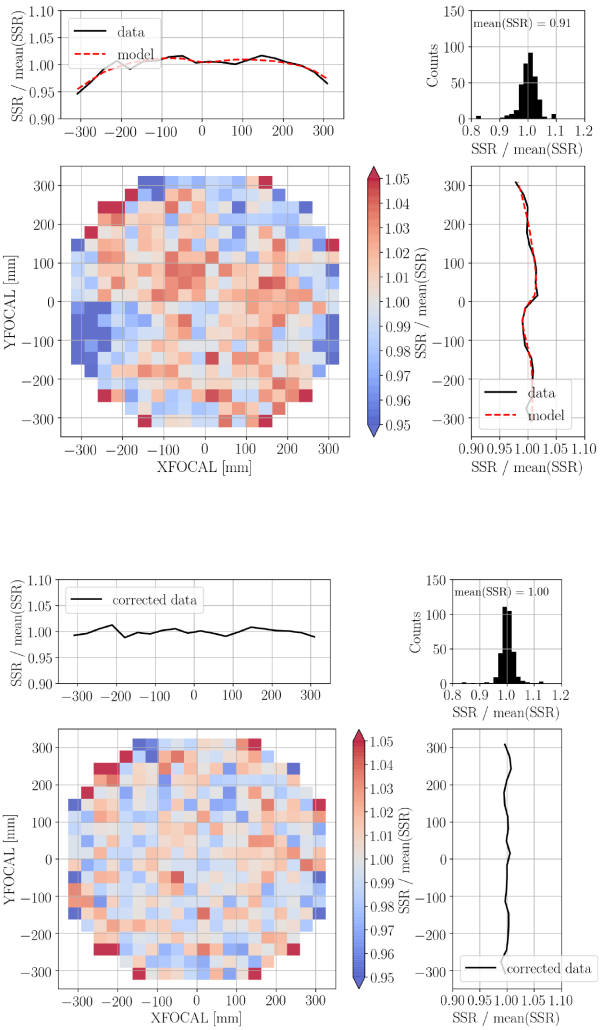

Figure 5. Same as Fig. 4, but for the SGC.

have shown (their table 5) that the uncertainty in the modelling of redshift failures has a subdominant impact on the clustering measurements.

The total redshift failure weight $w_{\rm noz}$ applied on the data is the inverse product of $f_{\rm noz,pSN}$ and $f_{\rm noz,XYFOCAL}$. To avoid double counting redshift failures, we weight each object by the median SN correction to perform the (XFOCAL,YFOCAL) fit (equation 7).

3.4 Fibre collision and tiling completeness

When two or more targets are closer than the fibre collision radius (62 arcsec on the sky), they cannot not be spectroscopically observed within a single plate. Those targets are said to 'collide' and form what we call a 'collision group' (see Blanton et al. 2003; Reid et al. 2016, for more details). This effect has to be corrected in the analysis, as it artificially changes the clustering of the sample. We weight each ELG with a valid fibre by the collision pair weight $w_{\rm cp}$ given by the number of targets over the number of valid fibres within each collision group. Collided or not valid fibres are declared resolved when they lie in the same collision group as an ELG valid fibre (see also Mohammad et al. 2020).

The tiling completeness COMP_BOSS is defined as the ratio of the number of resolved fibres to the number of targets in each sector, a sector being a region defined by a unique set of overlapping plates. The tiling completeness is included in the randoms systematic weight $w_{\rm sys}$ and can be seen in Fig. 1.

3.5 Systematics due to photometry

Once corrected for systematics related to spectroscopic observations ($w_{\rm noz}$ and $w_{\rm cp}$), our $0.6 < z_{\rm spec} < 1.1$ data sample still has (angular) imprints of the photometry used for target selection that need to be corrected for. First, in regions with shallow imaging, higher photometric noise implies that more $z_{\rm spec} < 0.6$ objects than $z_{\rm spec} > 0.6$ objects enter our selection box in the grz diagram, because of the density gradient in that grz diagram; we thus expect to have less $0.6 < z_{\rm spec} < 1.1$ objects in shallow imaging regions. Other regions where we expect to have less $0.6 < z_{\rm spec} < 1.1$ objects overall are regions with high Galactic extinction (because objects are dimmer) or regions with high stellar density (because each star is likely to blend with an ELG, which was not selected).

We include the following systematic photometric quantities as a source of systematics: the DECaLS imaging depth (`galdepth`, 5σ detection limit for a galaxy with an exponential profile with a radius of 0.45 arcsec) and seeing (`psfsize`) for the three grz bands, the stellar density (estimated from *Gaia*/DR2), and the Galactic extinction, using E(B−V), dust temperature (Schlegel et al. 1998), and the HI column density (HI4PI Collaboration 2016; Lenz, Hensley & Doré 2017).

We here describe the method to compute the $w_{\rm sys}$ weights that correct for the systematics coming from the imaging used for the target selection and from Galactic foregrounds. We first apply the veto masks both to our data and random samples. We split the sky in `Healpix` pixels with `nside` = 256 (area ~ 0.05 deg^2). For each pixel p, we firstly compute the median value $s_{\rm p}$ for each photometric quantity. Then, we compute $n_{\rm dat,p}$, the number of data weighted by $w_{\rm noz} \cdot w_{\rm cp}$, i.e. the number of $0.6 < z_{\rm spec} < 1.1$ ELGs corrected for spectroscopic biases. The number of randoms weighted by COMP_BOSS, $n_{\rm ran,p}$, is obtained to derive the effective fractional area of each pixel. For each chunk, we proceed to a multilinear fitting with minimizing the $\chi^2_{\rm chunk}$ defined as:

$$\chi^2_{\rm chunk} = \sum_{p \in {\rm P}} \left[\frac{n_{\rm dat,p} - n_{\rm ran,p} \cdot (\epsilon + \sum_{s \in {\rm S}} c_s \cdot s_{\rm p})}{\sigma_{\rm p}} \right]^2, \quad (8)$$

where P is the list of the `Healpix` pixels inside the considered chunk, S is the list of the photometric templates, $\sigma_{\rm p} = \sqrt{n_{\rm ran,p}}$ is the Poissonian error, and (ϵ, $c_{\rm s}$) are the fitted parameters. We present in Fig. 6 the fitted $c_{\rm s}$ per chunk, the error bars being estimated from the 1000 fit results on the EZmocks with systematics (Section 4.2). Overall, the fitted $c_{\rm s}$ agree at the 1–2σ level across the four chunks, except for the stellar density, where the `eboss21` chunk has a significantly lower coefficient; this could be explained by the fact that the stellar density spans significantly higher values in `eboss21` than in the other three chunks. We can then use the (ϵ, $c_{\rm s}$) fitted parameters to define the weight for each `Healpix` pixel p:

$$w_{\rm sys,p} = \frac{1}{\epsilon + \sum_{s \in S} c_{\rm s} \cdot s_{\rm p}}. \quad (9)$$

Figs 7 and 8 display the dependency of the ELG density for each systematics s before (red) and after (blue) applying the computed $w_{\rm sys}$, for the NGC and SGC, respectively. We see that our computation reduces the density variations where they are the strongest, e.g. for `psfsize` or the stellar density in the NGC.

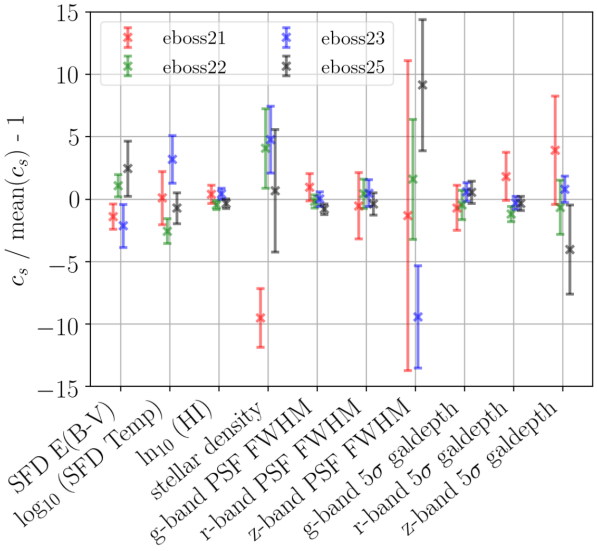

Figure 6. Per-chunk fitted coefficients c_s to define the w_{sys} weights (equation 8). For each systematic photometric quantity, the c_s are normalized to the mean over the four chunks. The error bars are estimated from the EZmocks with systematics described in Section 4.2.

We refer the interested reader to Kong et al. (2020), who find consistent results with a fully independent method. Their approach, developed in the DESI context and tested on the eBOSS/ELG sample, consists in injecting fake, realistic sources in the imaging itself, running the `legacypipe` photometric pipeline on it, and then applying the target selection. The strength of that approach is that it naturally accounts for any possible imaging systematics due to imaging.

3.6 Weight normalization

The mean of photometric weights w_{sys} of all ELG targets is normalized to 1 in each chunk. w_{noz} is then scaled such that the mean of the data completeness weights $w_{sys} \cdot w_{cp} \cdot w_{noz}$ of ELGs with a reliable redshift or stars (the latter being assigned $w_{noz} = 1$) is equal to the mean of w_{sys} over all resolved fibres. Then targets with collided or invalid fibres are assigned $w_{cp} = 0$. Objects that have an unreliable redshift or stars are assigned $w_{noz} = 0$.

3.7 Random redshifts and weights

Once cut over the chunk footprint and the angular veto masks, the randoms have the same angular distribution as data. We then need to attribute to the randoms redshifts with a similar radial distribution as the data. We assign redshifts to randoms following the *shuffled* scheme, i.e. picking up z_{spec} values from the data, with a probability proportional to $w_{noz} \cdot w_{cp} \cdot w_{sys}$, so that the weighted distributions of data and randoms match.

However, we need to account for another effect. The ELG data $n(z)$ depends on the depth of the imaging used for target selection (markedly for `eboss23`, but also in the SGC), with $n(z)$ having more $z_{spec} < 0.8$ ELGs in shallow imaging regions. Fig. 9 illustrates that effect for the r-band imaging in `eboss23`, where the sample is split in three bins of r-band imaging depth. This implies an angular–radial relation that needs to be accounted for in the randoms.

To account for this effect of depth on the target selection process, we split each chunk in three subregions of approximately constant imaging depth and apply the *shuffled* scheme in each subregion. We define the three subregions with modelling the $n(z)$ as a simple function of flux limits. We first define, at any position in the chunk, f_{grz}, a combined grz-band imaging depth that correlates best with the data z_{spec}. We define $f_{grz} = \epsilon + c_g f_g + c_r f_r + c_z f_z$, a linear combination

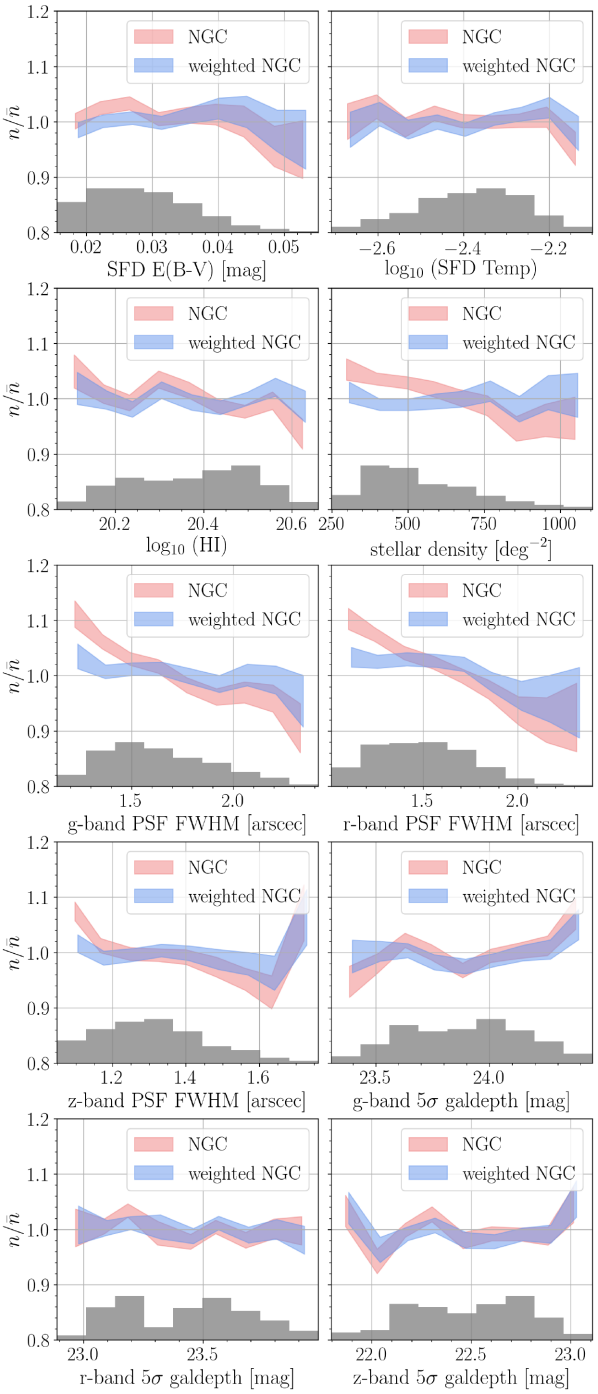

Figure 7. Density fluctuations in the NGC for the $0.6 < z_{spec} < 1.1$ ELGs with a reliable z_{spec}, weighted by $w_{noz} \cdot w_{cp}$, before (red) and after (blue) applying the w_{sys} weights. The systematics are: E(B–V) and dust temperature, H I column density, stellar density (from *Gaia*/DR2), grz-band imaging seeing, grz-band imaging depth. In each panel, we also display with the filled grey histogram the distribution of systematics values over the considered cap.

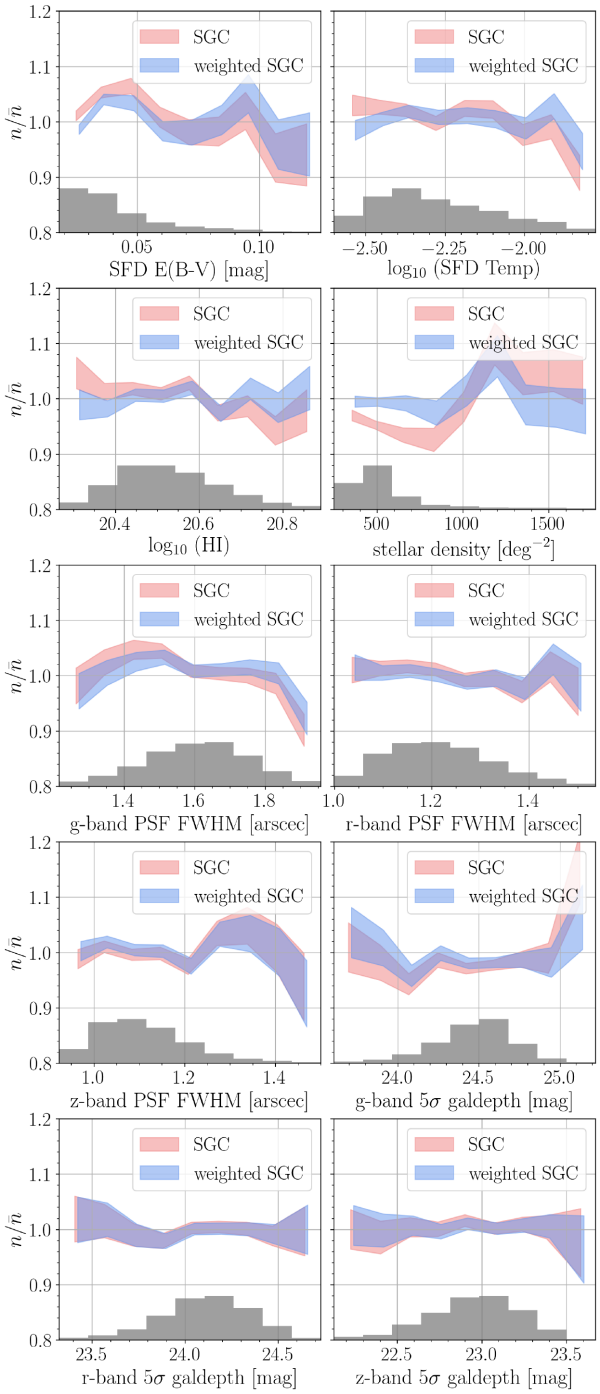

Figure 8. Same as Fig. 7, but for the SGC.

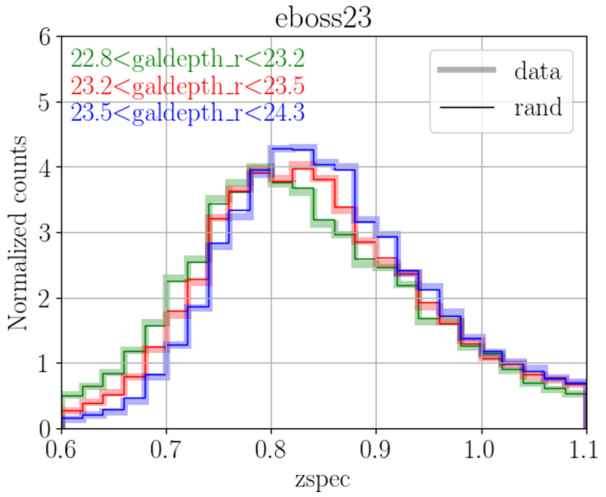

Figure 9. Illustration of the dependency of redshift distribution on imaging depth for the `eboss23` chunk, where the dependency is strong. Our randoms (thin lines) faithfully reproduce the trend of the data (thick lines).

of f_g, f_r, f_z, the 5σ flux detection limits of the imaging at the position of an ELG in the g-, r-, z-bands. The (ϵ, c_g, c_r, c_z) coefficients are the fitted with minimizing:

$$\chi^2_{grz} = \sum_{i=1}^{N_g} \left[z_{\mathrm{spec},i} - \left(\epsilon + c_g f_g^i + c_r f_r^i + c_z f_z^i\right)^2 \times w_{\mathrm{noz}}^i \cdot w_{\mathrm{cp}}^i \cdot w_{\mathrm{sys}}^i, \right. \quad (10)$$

where the sum is over the N_g ELGs of the chunk. We then bin the randoms in three bins of f_{grz}, hence defining the three subregions of approximately constant depth imaging[20]; the data are binned with the same three subregions. For a random with a f_{grz} value, we pick a redshift from the data z_{spec} from the corresponding f_{grz} bin, with a probability proportional to $w_{\mathrm{noz}} \cdot w_{\mathrm{cp}} \cdot w_{\mathrm{sys}}$. That approach allows us to reproduce this dependency in the randoms redshifts, as can be seen in Fig. 9, where the randoms weighted $n(z)$ closely follows that of the data when splitting by r-band imaging depth. We note that no significant $n(z)$ dependence is found with the other systematics (listed in Section 3.5); only a very mild dependence with `psfsize_g` and `psfsize_r` for `eboss23` is seen in the data, but a similar trend is seen in the randoms, meaning that it is mainly driven by the dependence with the `depth`.

For randoms, weights are defined as follows: w_{sys} is the tiling completeness COMP_BOSS, and $w_{\mathrm{noz}} = w_{\mathrm{cp}} = 1$. Then, random weights are normalized to ensure that the sum of weighted data over the sum of weighted randoms is the same in each `chunk_z`.

Using the *shuffled* scheme introduces a radial integral constraint (de Mattia & Ruhlmann-Kleider 2019), which is particularly important for this sample, as the random $n(z)$ is tuned to the data $n(z)$ in small chunks. We correct for that effect with using the formalism introduced in de Mattia & Ruhlmann-Kleider (2019). Zhao et al. (2020a) and Tamone et al. (2020) study the impact of that correction for the different multipoles, for the mocks and the data, respectively. The monopole is marginally changed, whereas the quadrupole and the hexadecapole are significantly changed.

Lastly, we remove 163 randoms belonging to tiny sectors where there are no data with a reliable z_{spec}, which is equivalent to restricting to sectors with `COMP_BOSS`$\geq$0.5 and SSR$\geq$0.

3.8 FKP and redshift distribution

As in previous BOSS/eBOSS analyses (e.g. Anderson et al. 2014; Alam et al. 2017; Ata et al. 2018), we define inverse-variance w_{FKP} weights to be applied to data and randoms. We define $w_{\mathrm{FKP}} = 1/(1 + n(z) \cdot P_0)$ (Feldman, Kaiser & Peacock 1994), where $P_0 = 4000$ $(\mathrm{Mpc}/h)^3$ is the amplitude of the power spectrum at $k \sim 0.1\,h\,\mathrm{Mpc}^{-1}$, a scale at which the FKP weights minimize the variance of the

[20]Those regions are identified by the `chunk_z` quantity in the catalogues.

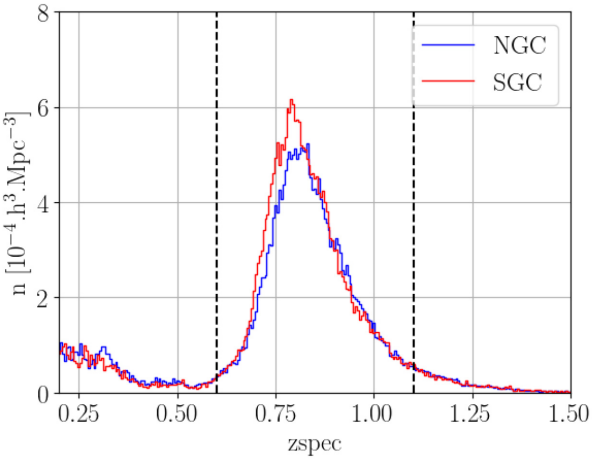

Figure 10. Number density of ELGs in the eBOSS survey. The vertical dashed lines indicate the redshift range used in our clustering measurement.

Table 6. Different cosmologies and redshift used in this paper. h is defined such that $H_0 = 100 \times h$ km s^{-1}Mpc^{-1}. All cosmologies are flat ΛCDM, hence $\Omega_\Lambda = 1 - \Omega_m$. The BAO fits in Section 5 are performed with the 'DR16 Fiducial' cosmology.

	DR16 fiducial	OuterRim	EZmocks
h	0.676	0.71	0.6777
Ω_m	0.31	0.26479	0.307115
$\Omega_b h^2$	0.022	0.02258	0.02214
σ_8	0.8	0.8	0.8225
n_s	0.97	0.963	0.9611
Σm_ν (eV)	0.06	0	0
Redshift	$z_{eff} = 0.845$	$z_{snap} = 0.865$	$z_{eff} = 0.845$

measurement and thus optimize the BAO measurement (Font-Ribera et al. 2014). Since $n(z)$ varies with the local clustering, the w_{FKP} weights tend to upweight (resp. down-weight) underdensities (resp. overdensities). We did verify that the induced systematic bias is small enough for our analysis.

The redshift distribution of our ELG sample, split by NGC and SGC, is displayed in Fig. 10. The effective redshift of our sample is $z_{eff} = 0.845$; as in other eBOSS analyses, z_{eff} is defined as the weighted mean spectroscopic redshift of galaxy pairs (z_i, z_j): $z_{eff} = \frac{\sum_{i,j} w_{tot,i} w_{tot,j} (z_i + z_j)/2}{\sum_{i,j} w_{tot,i} w_{tot,j}}$, where $w_{tot} = w_{sys} \cdot w_{cp} \cdot w_{noz} \cdot w_{FKP}$ and the sum are performed over all galaxy pairs between 25 h^{-1} Mpc and 120 h^{-1} Mpc.

We use the fiducial eBOSS DR16 cosmology (reported in Table 6) to derive the comoving number density.

3.9 Effects of weights on the monopole

We display in Fig. 11 how the weights computed in the previous sections change the clustering of the ELG sample. As expected (see e.g. Ross et al. 2017; Ata et al. 2018), the w_{sys} weights have by far the strongest impact on the clustering. We notice that the w_{cp} weights have an impact at all scales in the SGC and decreasing the clustering: a possible interpretation is the ELG SGC chunk geometry, noticeably `eboss21` with its small area. Close pairs should have been missed preferentially around the edges and there are more edges because of the small footprint. Lastly, the w_{noz} weights have a marginal impact on the clustering.

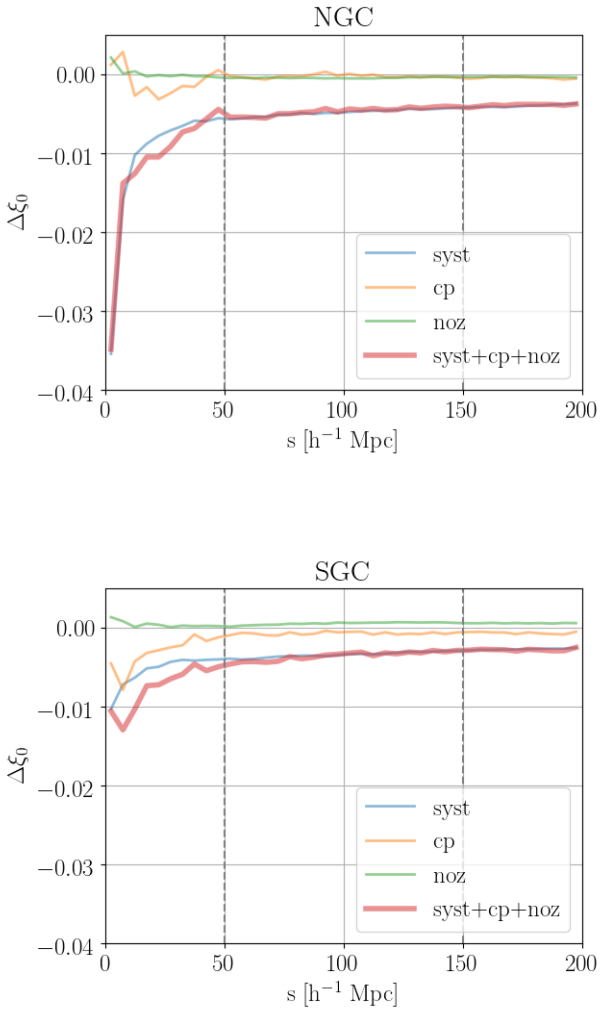

Figure 11. Effect of the weights on the clustering for the NGC (top panel) and the SGC (bottom panel). The vertical lines show the BAO fitting range in this paper.

4 MOCK CATALOGUES

In order to validate and perform our BAO fitting method, we rely on two sets of mock catalogues. The cosmology of each set of mock is reported in Table 6. We refer the reader to de Mattia et al. (2020) for more details on those both sets of mocks.

4.1 Accurate *N*-body Sky-cut OuterRim mocks

The first set of mock catalogues used in the subsequent BAO analysis is the Sky-cut OuterRim mocks, described in de Mattia et al. (2020). The starting product is the OuterRim simulation (Heitmann et al. 2019), which is one of the largest high-resolution *N*-body simulations to date, as it contains $10\,240^3$ particles with a mass of $1.85 \cdot 10^9$ h^{-1} $M_\odot$ over a volume of $(3000\ h^{-1}\ \mathrm{Mpc})^3$. Avila et al. (2020) have extracted from the OuterRim simulation the snapshot at $z_{snap} = 0.865$ and have produced accurate mocks, which faithfully reproduce the DR16 ELG data sample small-scale clustering, using the Halo Occupation Distribution modelling motivated by Gonzalez-Perez et al. (2018). From those Avila et al. (2020) mocks, the Sky-cut OuterRim mocks are generated by cutting the eBOSS/ELG footprint, applying the veto masks, and reproducing the data $n(z)$ distribution

and accounting for the $n(z)$ dependence with the imaging depth. Precisely, six nearly independent Sky-cut mocks are extracted from the OuterRim box; then, from each of those six mocks, we can extract four disjoint ELG-like samples and use three line of sight for each sample.

We thus have 72 Sky-cut mocks overall but with only six of them being almost fully uncorrelated. However, the correlation between the other Sky-cut mocks is not problematic for our analysis, as we use the Sky-cut mocks to have a representative, mean signal expected from our ELG sample (see Section 5.5).

4.2 Approximate EZmocks

The second set of mocks consists of the 1000 EZmocks realizations presented in Zhao et al. (2020a). The EZmocks are using the Zel'dovich approximation (Zel'Dovich 1970) to generate a density field and populate galaxies according to the desired tracer bias. As for the Sky-cut OuterRim mocks, those EZmocks are cut according to the eBOSS/ELG footprint, have the veto masks applied, reproduce the data $n(z)$ distribution, and account for the dependence with the imaging depth.

Additionally, we build another set of 1000 EZmocks, where we include the observational systematics present in the data. The method, briefly summarized below, is described in details in de Mattia et al. (2020) to which we refer the interested reader. Angular systematics are implemented with trimming the mocks – produced at a density higher than the ELG one – according to a smoothed map of the data observed density, and with adding contaminants (stars or objects outside $0.6 < z < 1.1$), so that the data target density is reproduced on average. Spectroscopic systematics are then implemented with introducing realistic fibre collisions (following the plate geometry and target priority) and redshift failures (using the nearest neighbour in the data). For each mock, we then compute the weighting scheme as we do for the data. We remark that, since weights are recomputed on each mock, the noise in the weight calculation due to shot noise and cosmic variance is automatically propagated to the final cosmological parameters.

Those EZmocks with observational systematics are the ones used in Section 5, in particular, to estimate the covariance matrices. The set of EZmocks without systematics is used only in Section 5.5, when comparing to the OuterRim mocks, which have no systematics included.

5 THE MODEL AND FITTING METHODOLOGY

5.1 The model

We measure spherically averaged BAO measurements using the 2-point correlation function. Our methodology closely follows that described in Anderson et al. (2014), Ross et al. (2017), Ata et al. (2018), and references therein, to which we refer for more details.

We first compute $\xi(s,\ \mu)$, the redshift-space 2D correlation function as a function of s, the separation vector in redshift space, and μ the cosine of the angle between s and the line-of-sight direction. We use the Landy & Szalay (1993) estimator:

$$\xi(s,\mu) = \frac{\mathrm{DD}(s,\mu) - 2\mathrm{DR}(s,\mu) + \mathrm{RR}(s,\mu)}{\mathrm{RR}(s,\mu)}, \tag{11}$$

where DD, DR, and RR are the normalized number of data–data, data–random, random–random pairs with a separation of s and an orientation of μ.[21] We then compute the monopole correlation function $\xi_0(s)$, i.e. the first Legendre multipole with:

$$\xi_l(s) = \frac{2l+1}{2} \int_{-1}^{1} L_l(\mu)\xi(s,\mu)d\mu \quad \text{for} \quad l = 0, \tag{12}$$

where $L_l(\mu)$ is the l^{th}-order (0^{th} here) Legendre polynomial.

We measure the difference in the BAO location between our clustering measurement and that expected in our fiducial cosmology, which can mostly come either from a difference in projection or from the difference between the BAO position in the true intrinsic primordial power spectrum and that in the model, with the multiplicative shift depending on the ratio $r_{\mathrm{drag}}/r_{\mathrm{drag}}^{\mathrm{fid}}$, where r_{drag} is the comoving sound horizon at $z = z_{\mathrm{drag}}$, the redshift at which the baryon-drag optical depth equals unity (Hu & Sugiyama 1996). If we define the spherically averaged distance $D_V(z) = \left[D_M^2(z)\cdot cz H(z)^{-1}\right]^{1/3}$ as a combination of the Hubble parameter $H(z)$ and the comoving angular diameter distance $D_M(z)$, we can express the offset between the observed BAO location and our template as:

$$\alpha = \frac{D_V(z) r_{\mathrm{drag}}^{\mathrm{fid}}}{D_V^{\mathrm{fid}}(z) r_{\mathrm{drag}}}. \tag{13}$$

Once we have our measurement of α, it can be converted to an angular location of the BAO, a dimensionless quantity that is independent of the cosmology:

$$\frac{D_V(z_{\mathrm{eff}}=0.845)}{r_{\mathrm{drag}}} = \alpha \frac{D_V^{\mathrm{fid}}(z_{\mathrm{eff}}=0.845)}{r_{\mathrm{drag}}^{\mathrm{fid}}}. \tag{14}$$

For our fiducial cosmology ('DR16 Fiducial' in Table 6), $r_{\mathrm{drag}}^{\mathrm{fid}} = 147.77$ Mpc (obtained from CAMB;[22] Lewis, Challinor & Lasenby 2000; Howlett et al. 2012) and $D_V^{\mathrm{fid}}(z_{\mathrm{eff}}=0.845) = 2746.8$ Mpc.

We generate a template BAO feature using the linear power spectrum, $P_{\mathrm{lin}}(k)$, obtained from CAMB and a 'no-wiggle' $P_{\mathrm{nw}}(k)$ obtained from the Eisenstein & Hu (1998) fitting formulae,[23] both using our fiducial cosmology (except where otherwise noted).

Given $P_{\mathrm{lin}}(k)$ and $P_{\mathrm{nw}}(k)$, we account for RSD and non-linear BAO damping via

$$P(k,\mu) = C^2(k,\mu,\Sigma_s)\left((P_{\mathrm{lin}} - P_{\mathrm{nw}})e^{-k^2\sigma_v^2} + P_{\mathrm{nw}}\right., \tag{15}$$

where

$$\sigma_v^2 = (1-\mu^2)\Sigma_\perp^2/2 + \mu^2\Sigma_{||}^2/2, \tag{16}$$

$$C(k,\mu,\Sigma_{\mathrm{s}}) = \frac{1+\mu^2\beta(1-S(k))}{(1+k^2\mu^2\Sigma_{\mathrm{s}}^2/2)}. \tag{17}$$

$S(k)$ is the smoothing applied in reconstruction: $S(k) = e^{-k^2\Sigma_r^2/2}$ and $\Sigma_{\mathrm{r}} = 15\,h^{-1}$ Mpc for the reconstruction applied to the eBOSS ELG sample (see Section 5.3); $S(k) = 0$ for pre-reconstruction. This matches the implementation of Ross et al. (2017), which was motivated by Seo et al. (2016). For our fiducial analysis, we fix $\beta = 0.593$ and $\Sigma_{\mathrm{s}} = 3\,h^{-1}$ Mpc. Given this is a spherically averaged analysis that does not consider how the signal changes with respect

[21] The pair-counting is done using the 'DR16 Fiducial', 'OuterRim', and 'DR16 Fiducial' cosmology for the data, the OuterRim mocks, and the EZmocks, respectively.

[22] https://camb.info/

[23] In order to best match the broad-band shape of the linear power spectrum, we use $n_s = 0.963$, to be compared to 0.97 when generating the full linear power spectrum from CAMB. This linear power spectrum is same as used for BOSS and eBOSS galaxy analyses since DR11.

to the line of sight, we expect these parameters to have no significant effect. We use $\Sigma_\perp = 3\,h^{-1}$ Mpc and $\Sigma_{||} = 5\,h^{-1}$ Mpc for post-reconstruction results and $\Sigma_{||} = 10\,h^{-1}$ Mpc and $\Sigma_\perp = 6\,h^{-1}$ Mpc for pre-reconstruction. These values for the damping parameters are motivated, and further discussed, by results from Section 5.5, where we present results achieved from mock catalogues.

In order to produce our spherically averaged BAO template in the configuration space, $\xi_{\rm temp}$, we use the Fourier transform of $P_0(k) = {\rm d}\mu P(k, \mu)$. We then fit the model:

$$\xi_{\rm mod}(s, \alpha) = B\xi_{\rm temp}(s\alpha) + A_0 + A_1/s + A_2/s^2. \quad (18)$$

As in previous SDSS studies (e.g. Anderson et al. 2014; Ross et al. 2015, 2017) we use for B a Gaussian prior on $\log(B)$, with a width of 0.4 and centred on $B_{\rm fit}$, where $B_{\rm fit}$ is the value of B one obtains from the first measurement bin in the ξ_0 data vector ($50 < s < 55\,h^{-1}$ Mpc in our fiducial case) when fixing $A_N = 0$. The best-fitting A_N are analytically determined for each α grid-point, without restriction on their values.

In addition to damping the BAO oscillations, non-linear evolution effects are also expected to cause small shifts (of order 0.5 per cent) in the BAO position (Padmanabhan & White 2009), which should have a small cosmological dependence (e.g. the size of the shift is likely dependent on σ_8). Reconstruction has been demonstrated to reverse such effects and we will discuss any residual systematic uncertainty in Section 5.5.

5.2 Parameter estimation

As in Ata et al. (2018), we assume for the fitted data that the likelihood distribution, $\mathcal{L}$, of any parameter (or vector of parameters), p, of interest is a multivariate Gaussian:

$$\mathcal{L}(p) \propto e^{-\chi^2(p)/2}. \quad (19)$$

The χ^2 is given by the standard definition

$$\chi^2 = \mathbf{D}C^{-1}\mathbf{D}^T, \quad (20)$$

where C represents the covariance matrix of the measured correlation function and $\mathbf{D}$ is the difference between the data and model vectors, when model parameter p is used. Our DR16 fiducial cosmology (Table 6) is always used in the fits. We assume flat priors on all model parameters, unless otherwise noted. Our fitting range is $50 < s < 150\,h^{-1}$ Mpc, using $5\,h^{-1}$ Mpc bins for our fiducial $\xi(s)$ results. These choices match those applied in Ross et al. (2017), which were found to be appropriate for post-reconstruction data.

Similar to previous analyses (e.g. Ata et al. 2018), we obtain $\chi^2(\alpha)$ by finding the value of the nuisance parameters that minimizes $\chi^2(\alpha)$. We do this on a grid of spacing 0.001 in the range $0.8 < \alpha < 1.2$. We define a 'detection' as there being a $\Delta\chi^2 = 1$ region on both sides of the minimum χ^2. To report the results we use the Gaussian approximation that the uncertainty on the measurement as half of the width of this $\Delta\chi^2 = 1$ region and the maximum likelihood its mean. We recommend use of the full $\chi^2(\alpha)$ result for testing cosmological models, rather than this Gaussian approximation. This will be made publicly available after this work is accepted for publication.

In order to estimate covariance matrices, we use the 1000 approximate EZmocks with systematics included, which mimic our ELG sample (see Section 4.2). The noise from the finite number of mock realizations requires some corrections to the χ^2 values, the width of the likelihood distribution, and the standard deviation of any parameter determined from the same set of mocks used to define the covariance matrix. These factors are defined in Hartlap, Simon & Schneider (2007), Dodelson & Schneider (2013), and Percival et al. (2014); we apply the factors in the same way as in, e.g. Anderson et al. (2014) and Ata et al. (2018). For our fiducial $\xi(s)$ results, we use 1000 mocks and 20 measurement bins for each NGC and SGC regions. Thus, the number of mock realizations is much larger than the number of measurement bins, implying that the finite number of mocks has less than a 2 per cent effect on our uncertainty estimates.

5.3 Reconstruction

BAO measurements can be improved by applying 'reconstruction' techniques that partially remove non-linear effects on the BAO feature observed in 2-point clustering measurements (Eisenstein et al. 2007). We apply the reconstruction method presented in Burden, Percival & Howlett (2015) and further described in Bautista et al. (2018). The density field is estimated from the eBOSS/ELG sample alone, as the eBOSS LRG sample only partially covers the eBOSS ELG redshift range and NGC footprint. We use the case where RSD are removed and three iterations are applied. We assume that the ELG sample has a bias of 1.4 (approximately correct for our sample and fiducial cosmology), and we assume the growth rate $f = 0.82$. As in previous studies, we use a smoothing scale of $15\,h^{-1}$ Mpc. The particular parameters applied are not expected to bias the results (see e.g. Vargas-Magaña et al. 2018).

5.4 Comparing clustering in data and mocks

In Fig. 12, we display the spherically averaged redshift–space correlation functions we use for BAO measurements, compared to the mean of the EZmocks. The χ^2/degrees of freedom between the data and the mocks for the comparison are labelled in each panel of the figures. While we do expect these to be of order 1, some deviation is expected, given that the EZmocks are approximate and the fiducial EZmock cosmology is expected to be somewhat different than the true cosmology (in unknown directions, of course).

The pre-reconstruction results are shown in the top panel of Fig. 12. Immediately noticeable is the fact that the large-scale clustering amplitude is expected to be lower in the NGC compared to the SGC, and the results for the data are consistent with this expectation. The underlying effective bias model applied to the EZmocks is the same in both hemispheres. The difference in large-scale clustering amplitude is due to the fact that the $n(z)$ in the NGC is strongly dependent on the imaging depth and our treatment of this imparts an extra radial integral constraint. In the NGC, we also notice an excess of clustering at around $60\,h^{-1}$ Mpc; our only potential explanation for this is that it is a statistical fluctuation, as the overall agreement between the mocks and the data is reasonable (χ^2/degrees of freedom = 47.1/36). We notice an apparently strong BAO feature in the SGC data and no such feature in the NGC data.

The post-reconstruction results are shown in the middle panel of Fig. 12. The apparent BAO feature remains strong in the SGC data and missing from the NGC data. The pre-reconstruction excess at around $60\,h^{-1}$ Mpc in the NGC result has mostly been removed post-reconstruction, though the overall agreement has become slightly worse (χ^2/degrees of freedom = 50.6/36).

In the bottom-panel of Fig. 12, we compare the inverse-variance (based on the diagonal of the covariance matrix) weighted combination of the NGC and SGC to the mean of the EZmocks weighted in the same way. This demonstrates that the full sample agrees well with our expectations, over a range of scales $20 < s < 200\,h^{-1}$ Mpc that is significantly wider than we use for our BAO fits. However, given the differences between the NGC and SGC shown in the top

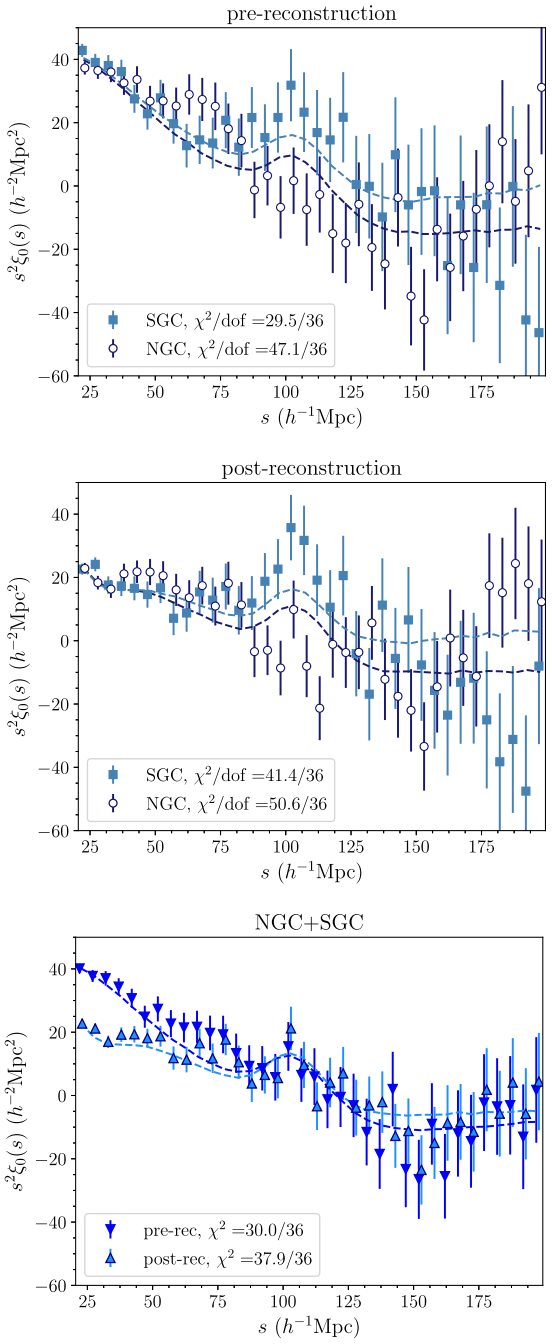

Figure 12. The measured DR16 correlation function of data ELGs (points with error bars) compared to the mean of the EZmocks (dashed lines). NGC and SGC are compared pre- and post-reconstruction in the top two panels. The bottom panel compares the NGC+SGC combination for both.

two panels and the fact that the $n(z)$-depth dependence for the data is much more severe in the NGC than in the SGC, we will fit the NGC and SGC separately and combine their likelihoods in order to obtain our BAO results.

The fact that the EZmocks reproduce the clustering of the eBOSS DR16 ELG sample, including the differences between the NGC and the SGC, suggests that they will provide a good covariance matrix for fitting the data. Further, the results suggest that applying our BAO fitting methodology to the EZmocks will provide a reasonably approximate statistical sample to interpret our fit to the data.

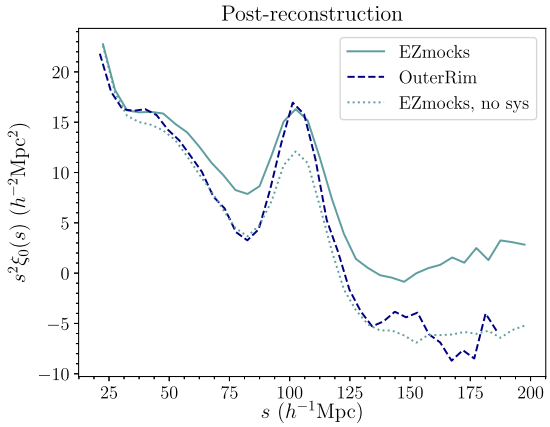

Figure 13. Comparison of the mean of the ELG EZ and OuterRim mocks in the SGC region. The OuterRim result has its s values scaled by $\alpha = 0.942$ in order to account for the difference in fiducial cosmologies.

5.5 Fitting mock catalogues

In this section, we present tests of BAO fitting methodology on mocks. We focus mostly on the post-reconstruction results. We will first investigate the results obtained from the mean of the EZ and OuterRim ELG mocks and then consider the results obtained from individual EZmock realizations.

As detailed in section 8.3 of Beutler et al. (2017), approximate mocks may not provide as sharp a BAO feature as expected (e.g. due to grid effects[24]) and one may wish to use N-body mocks to probe the expected signal strength. For this reason, BOSS DR12 used damping parameters motivated by the N-body results of Seo et al. (2016). Here, we use the Sky-cut OuterRim ELG mocks as N-body mock representing our expectations for the ELG sample.

Our tests on the OuterRim mocks predict a significantly stronger BAO feature than the EZmocks. Fig. 13 displays the mean of the post-reconstruction EZ and OuterRim mocks in the SGC region. The results for the EZmocks are shown with and without systematics imparted (the OuterRim mocks have no systematics imparted). The broad-band shapes are in good agreement when there are no systematics, but the BAO feature is significantly sharper for the OuterRim mocks. When systematic fluctuations are imparted, the broad-band amplitude is increased, but the sharpness of the BAO appears similar.

We investigate this further by fitting these mean ξ_0 with varying damping scales. The results are presented in Table 7. For each case, we use the covariance matrix of the EZmocks with systematic fluctuations. When systematic fluctuations are added to the EZmocks, the uncertainty that we obtain does not change (at the level of precision we quote); this indicates that indeed the BAO signal is nearly unaffected by the systematic fluctuations. These uncertainties are 50 per cent greater than those obtained from the OuterRim mocks. Relatedly, we find that the OuterRim mocks prefer smaller damping parameters than the EZmocks. The OuterRim mocks are well fit by damping parameters $\Sigma_\perp, \Sigma_{||} = 3, 5\,h^{-1}$ Mpc and we adopt these as our fiducial parameters to use for the data. Importantly, it is the observed BAO signal that strongly impacts the fit precision,

[24] A grid is used to compute the Zel'dovich approximation density field with Fast Fourier Transforms. The grid size ($\sim 5h^{-1}$ Mpc for the EZmocks) corresponds to a finite resolution of the displacement field: by applying this displacement field to dark matter particles, the clustering pattern can be smoothed, thus smearing out the BAO peak.

Table 7. Tests of BAO fits on the mean of ELG mocks. We quote the difference between the obtained α and that expected, given the cosmology of the mock, $\alpha_{\rm exp}$. For the EZmocks, $\alpha_{\rm exp} = 1.000$ and for OuterRim $\alpha_{\rm exp} = 0.942$. All results use the EZmock covariance matrices and the quoted uncertainty is for one realization (thus, the one should divide the uncertainty from the mean of the EZmocks by $\sqrt{1000}$ in order to compare to the total uncertainty). The χ^2 values for a given set of mocks are included only to allow one to determine the relative goodness-of-fit.

Case	$\alpha - \alpha_{\rm exp}$	χ^2
OuterRim mocks, post-reconstruction:		
$\Sigma_{\perp,\parallel} = 3, 5$	0.000 ± 0.025	0.36
$\Sigma_{\perp,\parallel} = 4, 7$	0.000 ± 0.026	0.50
EZmocks, post-reconstruction:		
$\Sigma_{\perp,\parallel} = 3, 5$	0.007 ± 0.038	0.23
$\Sigma_{\perp,\parallel} = 4, 7$	0.007 ± 0.040	0.11
$\Sigma_{\perp,\parallel} = 5, 8.5$	0.007 ± 0.042	0.10
EZmocks, post-reconstruction, no sys:		
$\Sigma_{\perp,\parallel} = 3, 5$	0.005 ± 0.038	0.08
$\Sigma_{\perp,\parallel} = 4, 7$	0.005 ± 0.040	0.04
$\Sigma_{\perp,\parallel} = 5, 8.5$	0.006 ± 0.042	0.09
EZmocks, pre-reconstruction:		
Fiducial	0.009 ± 0.055	0.11

rather than the signal assumed by the model (see for instance Hinton, Howlett & Davis 2020), i.e. the derived precision is only weakly dependent on the assumed $\Sigma_\perp$, $\Sigma_{||}$. This is illustrated by the fact that the greatest variation in the uncertainty that is obtained when varying the damping parameters is only 10 per cent (when changing from 3, 5 h^{-1} Mpc to 5, 8.5 h^{-1} Mpc) to be compared to the 50 per cent variation found above. The accuracy of the measurement is unaffected by this modelling choice, as $\alpha - \alpha_{\rm exp}$ changes by only 0.001.

The BAO measurement for the mean of the EZmocks is biased high, and given there are 1000 EZmocks, the significance is $>5\sigma$ for the mocks with systematic fluctuations. However, compared to the precision we achieve on the data, it is less than 0.25σ and thus not significant. Further, our results on the OuterRim simulation are unbiased, so it is unclear if it is our methodology or the nature of the approximate EZmocks causing the bias (especially given the same modelling techniques achieved unbiased results in the past). Some of the shift can be attributed to the systematic fluctuations, as there is a 0.2 per cent shift in α when the fluctuations are added.

Given that we expect the BAO signal to be stronger in the data than in the EZmocks, we therefore expect the uncertainty we achieve on the data to be better than the typical EZmock and closer to the OuterRim result. Even so, studying the distribution of mock results is an important validation of the methodology and allows comparisons to other ELG analyses. Given the strength of the BAO feature in the mean of the EZmocks, we use $\Sigma_{\perp,\parallel} = 4, 7h^{-1}$ Mpc as the fiducial choice for fitting individual EZmock realizations.

The pre- and post-reconstruction fits on the individual EZmocks are displayed in Fig. 14, and the results of the post-reconstruction fits to individual EZmock realizations are presented in Table 8. We consider that a fit provides a 'detection' if the $\Delta\chi^2 = 1$ region is within $0.8 < \alpha < 1.2$. The fiducial case has 'detections' for 963/1000 realizations. However, when considering the NGC-only or SGC-only, the fraction of realizations with 'detections' is significantly lower (887/1000 and 861/1000, respectively). Thus, 11 (14) per cent of the EZmocks do not have a 'detection' in the NGC (SGC), and 23 per cent of the EZmocks do not have a 'detection' in either NGC or SGC: de Mattia et al. (2020) find a similar fraction of no 'detections' in the individual NGC/SGC when analysing the EZmocks in the Fourier space.

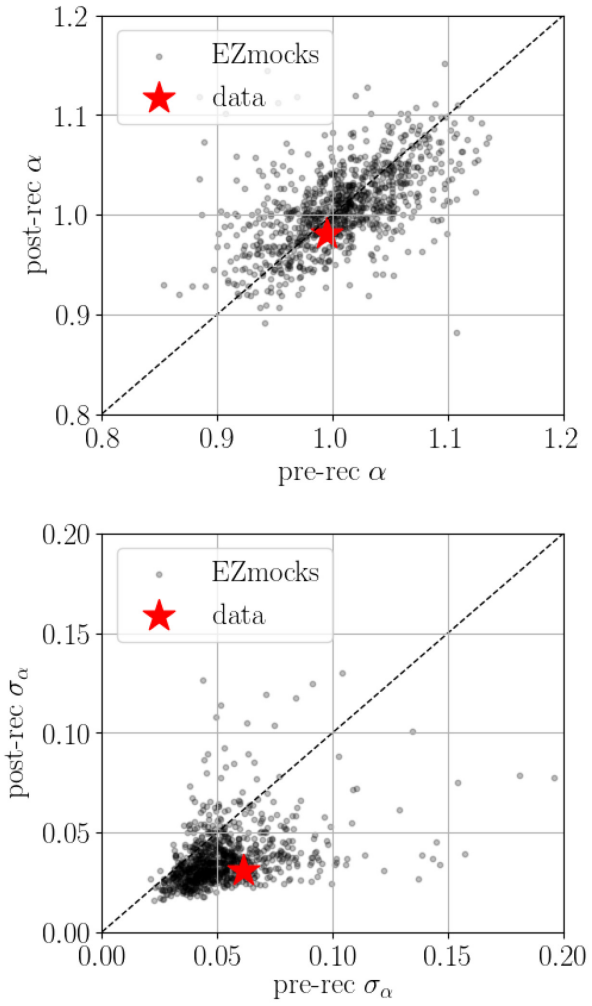

Figure 14. Comparison of the NGC+SGC pre- and post-reconstruction BAO fit results for the 1000 EZmocks (grey dots) and the data (red star). The top panel displays the α BAO parameter, and the bottom panel displays the uncertainty on α.

It has been demonstrated in previous works that slight improvement could be gained with combining fitting results using different bin centres, as those are not perfectly correlated (e.g. see section 4.3 from Anderson et al. 2014): we find that little gain is achieved by taking the mean result of the $\chi^2(\alpha)$ across the five bin centres. For the ease of reproducibility and sharing/comparing results, we will use bin centres with no shift (i.e. the first bin contains pairs with separation $0 < s < 5\,h^{-1}$ Mpc) as the fiducial result.

Lastly, combining first the NGC and SGC correlation functions and then fitting the combined $\xi(s)$ provides similar results.

5.6 BAO measurement from the DR16 ELG correlation function

We use the post-reconstruction DR16 ELG correlation function to obtain a 3.2 per cent measurement of $\frac{D_V(z_{\rm eff}=0.845)}{r_{\rm drag}} = 18.23 \pm 0.58$. This result is obtained from fitting the NGC and SGC results separately and adding their $\chi^2(\alpha)$. This quoted result is a Gaussian approximation to the full likelihood; any cosmological tests should

Table 8. Statistics for post-reconstruction BAO fits on the 1000 EZmocks. $\langle\alpha\rangle$ is the mean measured BAO parameter with 1σ bounds within the range $0.8 < \alpha < 1.2$. $\langle\sigma\rangle$ is the mean of the uncertainty obtained from $\Delta\chi^2 = 1$ region and S is the standard deviation of these α. $N_{\rm det}$ is the number of realizations with such 1σ bounds. The ξ bin size is $5h^{-1}$ Mpc, unless noted otherwise. Tests of shifting bin centres are noted by $+x$, with x representing the shift in h^{-1} Mpc. For these fits, we use damping parameters $\Sigma_{\perp,\parallel} = 4, 7h^{-1}$ Mpc unless otherwise noted. Results labelled 'combined' represent cases where the mean of the $\chi^2(\alpha)$ across five bin centres has been used. Results labelled 'combined $\xi(s)$' represent when first combining the NGC and SGC $\xi(s)$ before fitting.

Case (+bin shift)	$\langle\alpha\rangle$	$\langle\sigma\rangle$	S	$N_{\rm det}$	$\langle\chi^2\rangle$/degrees of freedom
EZmocks:					
Fiducial	1.008	0.040	0.042	963	31.8/31
+1	1.008	0.041	0.042	962	31.9/31
+2	1.008	0.040	0.043	953	31.9/31
+3	1.006	0.039	0.042	958	31.8/31
+4	1.008	0.040	0.042	963	31.8/31
Combined	1.008	0.040	0.041	961	31.9/31
$\Delta s = 8\,h^{-1}$ Mpc	1.006	0.040	0.043	955	18.2/17
$\Sigma_{\perp,\parallel} = 3, 5h^{-1}$ Mpc	1.008	0.038	0.042	965	31.9/31
NGC	1.005	0.051	0.048	887	15.4/15
SGC	1.006	0.054	0.054	861	15.4/15
Combined $\xi(s)$	1.008	0.041	0.041	962	15.4/15

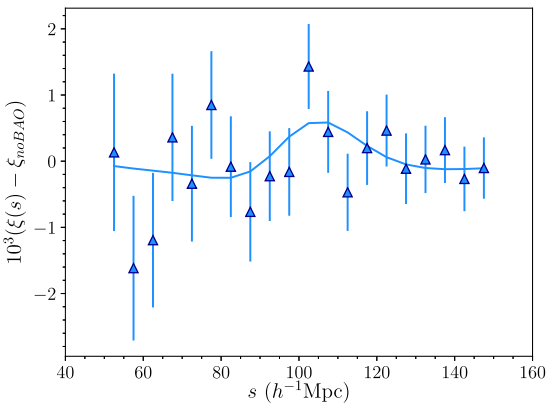

Figure 15. The NGC+SGC post-reconstruction correlation function compared to the best-fitting model, both with the smooth component of the model subtracted.

use the full non-Gaussian likelihood (discussed below). Our Gaussian approximation to the likelihood is to use the $\Delta\chi^2 = 1$ region as the 1σ width. The result is converted from $\alpha = 0.981 \pm 0.031$ (equation 14). The χ^2/degrees of freedom is slightly high, at 44.4/31, but a greater χ^2 is expected 5.6 per cent of the time under Gaussian expectations.

Fig. 15 displays the result of our BAO fit. Here, we subtract the smooth, 'no BAO' component of the best-fitting model from both the data and the total best-fitting model. We display the inverse variance weighted mean of the NGC and SGC results. The $\Delta\chi^2(\alpha)$ likelihood associated with this fit, i.e. the full non-Gaussian likelihood, is displayed in Fig. 16, using a solid curve (labelled ξ). It has a significant non-Gaussian component that becomes more pronounced far from the maximum likelihood. Also shown is the $\Delta\chi^2(\alpha)$ when using a template with no BAO feature, using dashed curves. There is only a mild ($\Delta\chi^2 < 1$) preference for the model with BAO. However,

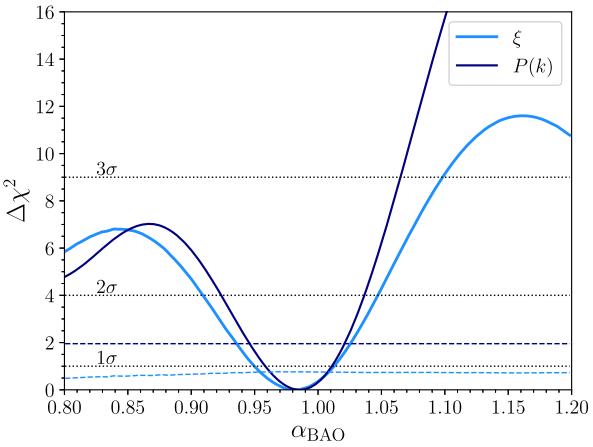

Figure 16. The BAO likelihood obtained from the combination of NGC and SGC results. We display our results (ξ) and also the Fourier-space ($P(k)$) results from de Mattia et al. (2020). The dashed curves show the results for the model with no BAO.

the no BAO model $\chi^2(\alpha)$ is nearly flat and has no local minima. Thus, the precision of our result is produced by the fact that, while a smooth model is not a significantly worse fit to the data, a model *with* a BAO far from the maximum likelihood is a significantly worse fit to the data. The a priori knowledge that the BAO feature is present in the clustering, now well established, justifies the validity of that approach and allows us to obtain a 3.2 per cent measurement, even if the model with a BAO feature is only mildly preferred by our ELG data.

Fig. 16 also displays the $\chi^2(\alpha)$ obtained from Fourier-space analysis in de Mattia et al. (2020) [labelled $P(k)$]. The results of the two studies are clearly consistent in terms of the location of the BAO feature, but the $P(k)$ results are more precise. The detailed tests presented in de Mattia et al. (2020) demonstrate the robustness of their result and we thus recommend that it is used for the DR16 ELG BAO measurement, given its increased statistical precision.

We present a series of robustness test in Table 9. The most notable results from the table are those that show that our measurements come almost entirely from the SGC data. This is not surprising, given the ξ_0 displayed in Fig. 12. It is not particularly surprising that the NGC data do not provide a BAO measurement on its own: we find the same in more than 10 per cent of the fits applied to the EZmocks. This would happen somewhat less if the BAO signal in the EZmocks was consistent with our assumed $\Sigma_{\perp,\parallel} = 3, 5h^{-1}$ Mpc. Given 3.7 per cent of the NGC+SGC fits to the EZmocks result in no BAO measurement, we believe that it would remain at least a 5 per cent probability. Conversely, we are somewhat lucky with the SGC result, as 9.2 per cent of the EZmocks have an uncertainty less than 0.033. This result would become more common if the EZmocks had a BAO signal consistent with $\Sigma_{\perp,\parallel} = 3, 5h^{-1}$ Mpc. This analysis suggests that our results are not particularly unusual. As expected from the fact that the NGC+SGC result is mostly driven by the SGC clustering, the SGC-only clustering provides $\alpha = 0.989 \pm 0.033$, in agreement with the NGC+SGC one.

As is typical for BAO measurements, the arbitrary choices in our analysis have a small effect on our measured α. Increasing the damping parameters to $\Sigma_{\perp,\parallel} = 4, 7h^{-1}$ Mpc (from 3, $5h^{-1}$ Mpc) decreases α by $<0.1\sigma$ but does increase the estimated uncertainty by 16 per cent. Using a flat prior on B ($B > 0$), instead of a Gaussian prior, shifts the result higher by $\sigma/3$. In this case, the NGC result prefers $B = 0$ at all α and result comes entirely from the SGC. A 0.55σ

Table 9. Results for BAO fits to the DR16 ELG data. The fiducial ξ case uses post-reconstruction data with $5h^{-1}$ Mpc bin size, centres in the range $50 < s < 150h^{-1}$ Mpc, $\Sigma_{\perp,||} = 3, 5h^{-1}$ Mpc, and $0.6 < z < 1.1$. Tests of shifting bin centres are noted by $+x$, with x representing the shift in h^{-1} Mpc; results labelled 'combined' represent cases where the mean of the $\chi^2(\alpha)$ across five bin centres has been used. Results labelled 'combined $\xi(s)$' represent when first combining the NGC and SGC $\xi(s)$ before fitting.

Measurement	$\frac{D_V(z_{\rm eff}=0.845)}{r_{\rm drag}} = 18.23 \pm 0.58$	
Robustness tests		
Case	α	χ^2/degrees of freedom
Post-recon. SGC+NGC:		
Fiducial	0.981 ± 0.031	44.4/31
$\Sigma_{\perp,\|\|} = 4, 7h^{-1}$ Mpc	0.979 ± 0.036	44.5/31
Flat prior on B	0.990 ± 0.030	37.4/33
$A_{\rm n} = 0$	0.964 ± 0.035	51.8/37
$A_{1,2} = 0$	0.964 ± 0.035	49.9/35
$A_2 = 0$	0.980 ± 0.033	47.6/33
$+A_3$	0.979 ± 0.034	42.9/29
$+1$	0.978 ± 0.033	50.1/31
$+2$	0.994 ± 0.034	42.4/31
$+3$	0.985 ± 0.031	39.4/31
$+4$	0.986 ± 0.029	44.0/31
Combined	0.985 ± 0.032	44.1/31
Combined $\xi(s)$	0.977 ± 0.034	24.0/15
$P(k)$ (de Mattia et al. 2020)	$0.986^{+0.025}_{-0.028}$	–
Sample variations:		
$z > 0.7$	0.983 ± 0.040	43.0/31
SGC	0.989 ± 0.033	17.2/15
NGC	no detection	18.8/15
Pre-recon.	0.995 ± 0.061	40.2/31

shift to a lower α value is observed when setting the polynomial terms to 0. Once the number of polynomial terms is increased to at least 2, the α result changes by less than 0.002. The result is also stable to better than 0.1σ if we cut the sample to $z > 0.7$ (though doing so increases the uncertainty by 29 per cent), or if we first combine the NGC and SGC $\xi(s)$ and fit that combined $\xi(s)$. Finally, the uncertainty is decreased by nearly a factor of 2 via the application of reconstruction, but the α value shifts by less than the decrease in the uncertainty. We conclude that, while there are aspects that might strike one as puzzling initially, the BAO measurements we extract from the sample are robust.

5.7 Comparison to other studies

We compare in Fig. 17 our isotropic BAO measurement with published values at redshifts close to our $z_{\rm eff}$. We normalize the values to the prediction for the best-fitting cosmological parameters for a ΛCDM model from the TT+TE+EE+lowE+lensing Planck Collaboration VI (2020) result.

First of all, our measurement is in very good agreement ($<0.2\sigma$) with the isotropic measurement made on the same eBOSS ELG sample in the Fourier space from de Mattia et al. (2020), with similar uncertainty. The eBOSS LRG consensus result from Bautista et al. (2020) at $z = 0.70$ combines the configuration space and Fourier space anisotropic analyses of ∼376 000 LRGs in $0.6 < z < 1.0$ selected with the SDSS and *WISE* imaging over 4200 deg^2 and provides a smaller uncertainty of 1.5 per cent. We also display the WiggleZ result at $z = 0.73$ from the isotropic analysis of ∼80 000 ELGs in the $0.6 < z < 1.0$ range selected with the *GALEX* UV

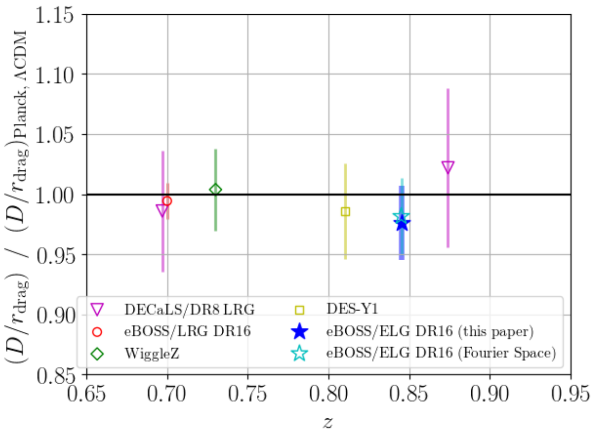

Figure 17. BAO distance measurements close to our $z_{\rm eff}$, normalized to the prediction from the Planck Collaboration VI (2020) ΛCDM best-fitting parameters. The considered distance D is D_V for all studies, except for the DES-Y1 and DECaLS/DR8 studies where it is D_A. See text for details.

imaging over 900 deg^2, which has a 3.4 per cent precision (Kazin et al. 2014). Lastly, we display two other results, which estimate the angular diameter distance $D_{\rm A}(z)/r_{\rm drag}$ with analysing the angular clustering of photometrically selected galaxy samples: DES reports a 4 per cent measurement at $z = 0.81$, using a sample of ∼1.3 million galaxies over 1300 deg^2 (Abbott et al. 2019); and Sridhar et al. (2020) obtain a 5.1, 6.5 per cent measurement at $z = 0.70, 0.87$ from 3 million galaxies over 9000 deg^2 selected from the DECaLS/DR8 release.

All current studies are consistent with the *Planck* prediction at the 1σ level or better. The diversity of the studies (spectroscopic or photometric samples, selection done with different imaging, different pipeline analysis) strengthens this overall agreement.

6 CONCLUSION

We have presented the eBOSS/ELG DR16 spectroscopic data, the construction of the LSS catalogues, and the spherically averaged BAO analysis in configuration space. The LSS catalogues are publicly available[25] and used in two companions papers analysing the anisotropic clustering of the sample, de Mattia et al. (2020, Fourier space) and Tamone et al. (2020, configuration space).

After having described the observations of the 269 243 ELG spectra over 1170 deg^2, we detailed the $z_{\rm spec}$ measurement procedure: thanks to pipeline improvements, the rate of redshift failures is decreased from 17 to 10 per cent, while simultaneously decreasing the rate of catastrophic redshifts (from 0.5 to 0.3 per cent), estimated from repeat observations and visual inspections.

We then described the construction of the LSS catalogues, which are required for the cosmological analyses. Unlike other eBOSS tracers selected on SDSS imaging, the ELGs have been selected on a preliminary release of the DECaLS imaging; as a consequence, the LSS construction requires a special attention. For the data, we restrict to the 173 736 ELGs with a reliable $z_{\rm spec}$ measurement with $0.6 < z_{\rm spec} < 1.1$. We extensively described the angular veto masks resulting from masking at the target selection step and a posteriori masking for ensuring reliable galaxy observations. We then defined the weights that correct for non-cosmological fluctuations;

[25] https://data.sdss.org/sas/dr16/eboss/lss/catalogs/DR16/

noticeably, the redshift failure correction accounts for the dependence on the observation conditions and on the instrumental patterns, which is significant due to the low SN of the ELG spectra. Another feature specific to that ELG sample we need to correct for is the dependence of the redshift distribution with the imaging depth: shallow imaging regions tend to have more contamination from low-redshift objects entering the selection *grz*-box; we account for that effect with an ad hoc method reproducing the effect in the randoms.

Lastly, we presented a spherically averaged BAO measurement on the reconstructed monopole. The ELG data present a strong BAO feature in the SGC and no significant BAO feature in the NGC; analysing 1000 approximate EZmocks suggests that this result is not particularly unusual. When combining the SGC and the NGC, the data have a feature consistent with that of the BAO, providing a 3.2 per cent measurement of $D_V(z_{\rm eff} = 0.845)/r_{\rm drag} = 18.23 \pm 0.58$.

The analysis presented in this paper, along with the ones presented in de Mattia et al. (2020) and Tamone et al. (2020), is likely to provide valuable tools in the ELG clustering analysis, paving the way for next-generation massive BAO surveys, which will mostly target ELGs, as DESI, PFS, *Euclid*, or *WFIRST*.

Authors contribution. AR led this paper, the supervising of the spectroscopic data acquisition, the generation of intermediate catalogues from the pipeline outputs, the validation of the `redrock` $z_{\rm spec}$ measurements, and the building of the veto masks and of the $w_{\rm sys}$ and $w_{\rm noz}$ weights. AdM led the generation of the LSS catalogues from intermediate catalogues, the implementation of systematics in the mocks, the implementation of the $n(z)$-depth dependence, and the building of the $w_{\rm cp}$ and $w_{\rm FKP}$ weights. AJR led the BAO fitting. CZ led the EZmocks realization. JB, KSD, and HdMdB produced the `redrock` ELG $z_{\rm spec}$ measurements. Other co-authors provided valuable input products or feedback for the analysis.

We thank the anonymous referee for her/his report, which helped us to improve the clarity of the paper.

ACKNOWLEDGEMENTS

AR and JPK acknowledge support from the ERC advanced grant LIDA. AR, CZ, and AT acknowledge support from the SNF grant 200020_175751. AdM acknowledges support from the P2IO LabEx (ANR-10-LABX-0038) in the framework 'Investissements d'Avenir' (ANR-11-IDEX-0003-01) managed by the Agence Nationale de la Recherche (ANR, France). AJR is grateful for support from the Ohio State University Center for Cosmology and Particle Physics. Authors acknowledge support from the ANR eBOSS project (ANR-16-CE31-0021) of the French National Research Agency. S. Alam is supported by the European Research Council through the COSFORM Research grant (#670193). S. Avila was supported by the MICUES project funded by the European Union's Horizon 2020 research programme under the Marie Sklodowska-Curie Grant Agreement No. 713366 (InterTalentum UAM). ADM was supported by the U.S. Department of Energy, Office of Science, Office of High Energy Physics, under Award number DE-SC0019022. VGP acknowledges support from the European Union's Horizon 2020 research and innovation programme (ERC grant #769130). JM gratefully acknowledges support from the U.S. Department of Energy, Office of Science, Office of High Energy Physics under award number DE-SC002008 and from the National Science Foundation under grant AST-1616414. EMM acknowledges support from the European Research Council (ERC) under the European Union's Horizon 2020 research and innovation programme (grant agreement no. 693024). GR acknowledges support from the National Research Foundation of Korea (NRF) through grants no. 2017R1E1A1A01077508 and no. 2020R1A2C1005655 funded by the Korean Ministry of Education, Science and Technology (MoEST), and from the faculty research fund of Sejong University.

Funding for the Sloan Digital Sky Survey IV has been provided by the Alfred P. Sloan Foundation, the U.S. Department of Energy Office of Science, and the Participating Institutions. SDSS acknowledges support and resources from the Center for High-Performance Computing at the University of Utah. The SDSS website is www.sdss.org.

SDSS is managed by the Astrophysical Research Consortium for the Participating Institutions of the SDSS Collaboration including the Brazilian Participation Group, the Carnegie Institution for Science, Carnegie Mellon University, the Chilean Participation Group, the French Participation Group, Harvard-Smithsonian Center for Astrophysics, Instituto de Astrofísica de Canarias, The Johns Hopkins University, Kavli Institute for the Physics and Mathematics of the Universe (IPMU)/University of Tokyo, the Korean Participation Group, Lawrence Berkeley National Laboratory, Leibniz Institut für Astrophysik Potsdam (AIP), Max-Planck-Institut für Astronomie (MPIA Heidelberg), Max-Planck-Institut für Astrophysik (MPA Garching), Max-Planck-Institut für Extraterrestrische Physik (MPE), National Astronomical Observatories of China, New Mexico State University, New York University, University of Notre Dame, Observatório Nacional/MCTI, The Ohio State University, Pennsylvania State University, Shanghai Astronomical Observatory, United Kingdom Participation Group, Universidad Nacional Autónoma de México, University of Arizona, University of Colorado Boulder, University of Oxford, University of Portsmouth, University of Utah, University of Virginia, University of Washington, University of Wisconsin, Vanderbilt University, and Yale University.

This paper presents observations obtained at Cerro Tololo Inter-American Observatory, National Optical Astronomy Observatory (NOAO Prop. ID: 2014B-0404; co-PIs: D. J. Schlegel and A. Dey), which is operated by the Association of Universities for Research in Astronomy (AURA) under a cooperative agreement with the National Science Foundation. This paper also includes DECam observations obtained as part of other projects, namely the Dark Energy Survey (DES, NOAO Prop. ID: 2012B-0001).

DECaLS used data obtained with the Dark Energy Camera (DECam), which was constructed by the Dark Energy Survey (DES) collaboration. Funding for the DES Projects has been provided by the U.S. Department of Energy, the U.S. National Science Foundation, the Ministry of Science and Education of Spain, the Science and Technology Facilities Council of the United Kingdom, the Higher Education Funding Council for England, the National Center for Supercomputing Applications at the University of Illinois at Urbana-Champaign, the Kavli Institute of Cosmological Physics at the University of Chicago,Center for Cosmology and Astroparticle Physics at the Ohio State University, the Mitchell Institute for Fundamental Physics and Astronomy at Texas A&M University, Financiadora de Estudos e Projetos, Fundação Carlos Chagas Filho de Amparo, Financiadora de Estudos e Projetos, Fundação Carlos Chagas Filho de Amparo à Pesquisa do Estado do Rio de Janeiro, Conselho Nacional de Desenvolvimento Científico e Tecnológico and the Ministério da Ciência, Tecnologia e Inovacão, the Deutsche Forschungsgemeinschaft, and the Collaborating Institutions in the Dark Energy Survey. The Collaborating Institutions are Argonne National Laboratory, the University of California at Santa Cruz, the University of Cambridge, Centro de Investigaciones Enérgeticas, Medioambientales y Tecnológicas-Madrid, the University of Chicago, University College London, the DES-Brazil Consortium, the University of Edinburgh, the Eidgenössische Technische Hochschule (ETH) Zürich, Fermi National Accelerator Laboratory, the University of Illinois at Urbana-Champaign, the Institut de Ciències de l'Espai (IEEC/CSIC), the

Institut de Física d'Altes Energies, Lawrence Berkeley National Laboratory, the Ludwig-Maximilians Universität München and the associated Excellence Cluster Universe, the University of Michigan, the National Optical Astronomy Observatory, the University of Nottingham, the Ohio State University, the University of Pennsylvania, the University of Portsmouth, SLAC National Accelerator Laboratory, Stanford University, the University of Sussex, and Texas A&M University.

This research used resources of the National Energy Research Scientific Computing Center, a DOE Office of Science User Facility supported by the Office of Science of the U.S. Department of Energy under contract no. DE-AC02-05CH11231.

This work used resources from the Sciama High Performance Computing cluster, which is supported by the Institute of Cosmology and Gravitation and the University of Portsmouth.

DATA AVAILABILITY

The LSS catalogues are publicly available: https://data.sdss.org/sas/dr16/eboss/lss/catalogs/DR16/. At the same address, we also provide the required information to reproduce the angular masking when considering any (R.A., Dec.) position: bits 1–7 can be computed with the `brickmask` script: https://github.com/cheng-zhao/brickmask/releases/tag/v1.0; bits 8–11 and the two `eboss22` low-quality plates can be reproduced with customed PYTHON lines, available on request.

REFERENCES

Abbott T. M. C. et al., 2019, MNRAS, 483, 4866
Addison G. E., Bennett C. L., Jeong D., Komatsu E., Weiland J. L., 2019, ApJ, 879, 15
Ahumada R. et al., 2020, ApJS, 249, 3
Alam S. et al., 2017, MNRAS, 470, 2617
Alam S. et al., 2020, preprint (arXiv:2007.09004)
Anderson L. et al., 2014, MNRAS, 441, 24
Ata M. et al., 2018, MNRAS, 473, 4773
Avila S. et al., 2020, MNRAS, 499, 5486
Bautista J. E. et al., 2017, A&A, 603, A12
Bautista J. E. et al., 2018, ApJ, 863, 110
Bautista J. E. et al., 2020, MNRAS, 500, 736
Beutler F. et al., 2017, MNRAS, 464, 3409
Blake C. et al., 2010, MNRAS, 406, 803
Blanton M. R., Lin H., Lupton R. H., Maley F. M., Young N., Zehavi I., Loveday J., 2003, AJ, 125, 2276
Blanton M. R. et al., 2017, AJ, 154, 28
Bolton A. S. et al., 2012, AJ, 144, 144
Burden A., Percival W. J., Howlett C., 2015, MNRAS, 453, 456
Cole S. et al., 2005, MNRAS, 362, 505
Colless M. et al., 2003, preprint (arXiv:astro-ph/0306581)
Comparat J., Kneib J.-P., Bacon R., Mostek N. J., Newman J. A., Schlegel D. J., Yèche C., 2013, A&A, 559, A18
Comparat J. et al., 2016, A&A, 592, A121
Dawson K. S. et al., 2013, AJ, 145, 10
Dawson K. S. et al., 2016, AJ, 151, 44
de Mattia A., Ruhlmann-Kleider V., 2019, J. Cosmology Astropart. Phys., 2019, 036
de Mattia A. et al., 2020, preprint (arXiv:2007.09008)
Delubac T. et al., 2015, A&A, 574, A59
DESI Collaboration, 2016a, preprint (arXiv:1611.00036)
DESI Collaboration, 2016b, preprint (arXiv:1611.00037)
Dey A. et al., 2019, AJ, 157, 168
Dodelson S., Schneider M. D., 2013, Phys. Rev. D, 88, 063537
Doré O. et al., 2018, preprint (arXiv:1804.03628)
Drinkwater M. J. et al., 2010, MNRAS, 401, 1429
du Mas des Bourboux H. et al., 2020, ApJ, 901, 153
eBOSS Collaboration, 2020, preprint (arXiv:2007.08991)
Eisenstein D. J., Hu W., 1998, ApJ, 496, 605
Eisenstein D. J. et al., 2001, AJ, 122, 2267
Eisenstein D. J. et al., 2005, ApJ, 633, 560
Eisenstein D. J., Seo H.-J., Sirko E., Spergel D. N., 2007, ApJ, 664, 675
Eisenstein D. J. et al., 2011, AJ, 142, 72
Feldman H. A., Kaiser N., Peacock J. A., 1994, ApJ, 426, 23
Flaugher B. et al., 2015, AJ, 150, 150
Font-Ribera A., McDonald P., Mostek N., Reid B. A., Seo H.-J., Slosar A., 2014, J. Cosmology Astropart. Phys., 2014, 023
Gaia Collaboration, 2018, A&A, 616, A1
Gao Y. et al., 2018, ApJ, 869, 15
Gil-Marín H. et al., 2020, MNRAS, 498, 2492
Gonzalez-Perez V. et al., 2018, MNRAS, 474, 4024
Gonzalez-Perez V. et al., 2020, MNRAS, 498, 1852
Górski K. M., Hivon E., Banday A. J., Wand elt B. D., Hansen F. K., Reinecke M., Bartelmann M., 2005, ApJ, 622, 759
Gunn J. E. et al., 2006, AJ, 131, 2332
Guo H. et al., 2019, ApJ, 871, 147
Hartlap J., Simon P., Schneider P., 2007, A&A, 464, 399
Heitmann K. et al., 2019, ApJS, 245, 16
HI4PI Collaboration, 2016, A&A, 594, A116
Hinton S. R., Howlett C., Davis T. M., 2020, MNRAS, 493, 4078
Høg E. et al., 2000, A&A, 355, L27
Hou J. et al., 2020, MNRAS, preprint (arXiv:2007.08998)
Howlett C., Lewis A., Hall A., Challinor A., 2012, J. Cosmology Astropart. Phys., 2012, 027
Hu W., Sugiyama N., 1996, ApJ, 471, 542
Huang C. et al., 2019, ApJ, 886, 31
Kaiser N., 1987, MNRAS, 227, 1
Kazin E. A. et al., 2014, MNRAS, 441, 3524
Kong H. et al., 2020, MNRAS, 499, 3943
Landy S. D., Szalay A. S., 1993, ApJ, 412, 64
Lang D., Hogg D. W., Mykytyn D., 2016, Astrophysics Source Code Library, record ascl:1604.008
Laureijs R. et al., 2011, preprint (arXiv:1110.3193)
Lenz D., Hensley B. S., Doré O., 2017, ApJ, 846, 38
Lewis A., Challinor A., Lasenby A., 2000, ApJ, 538, 473
Lilly S. J., Le Fevre O., Hammer F., Crampton D., 1996, ApJ, 460, L1
Lin S. et al., 2020, MNRAS, 498, 5251
Lyke B. W. et al., 2020, ApJS, 250, 8
Madau P., Dickinson M., 2014, ARA&A, 52, 415
Madau P., Pozzetti L., Dickinson M., 1998, ApJ, 498, 106
Mohammad F. G. et al., 2020, MNRAS, 498, 128
Morganson E. et al., 2015, ApJ, 806, 244
Myers A. D. et al., 2015, ApJS, 221, 27
Neveux R. et al., 2020, MNRAS, 499, 210
Newman J. A. et al., 2013, ApJS, 208, 5
Padmanabhan N., White M., 2009, Phys. Rev. D, 80, 063508
Palanque-Delabrouille N. et al., 2016, A&A, 587, A41
Percival W. J. et al., 2014, MNRAS, 439, 2531
Perlmutter S. et al., 1999, ApJ, 517, 565
Planck Collaboration VI, 2020, A&A, 641, A6
Prakash A. et al., 2016, ApJS, 224, 34
Raichoor A. et al., 2016, A&A, 585, A50
Raichoor A. et al., 2017, MNRAS, 471, 3955
Reid B. et al., 2016, MNRAS, 455, 1553
Rezaie M., Seo H.-J., Ross A. J., Bunescu R. C., 2020, MNRAS, 495, 1613
Riess A. G. et al., 1998, AJ, 116, 1009
Ross A. J., Samushia L., Howlett C., Percival W. J., Burden A., Manera M., 2015, MNRAS, 449, 835
Ross A. J. et al., 2017, MNRAS, 464, 1168
Ross A. J. et al., 2020, MNRAS, 498, 2354
Rossi G. et al., 2020, preprint (arXiv:2007.09002)
Ruan J. J. et al., 2016, ApJ, 825, 137
Schlegel D. J., Finkbeiner D. P., Davis M., 1998, ApJ, 500, 525

Seo H.-J., Beutler F., Ross A. J., Saito S., 2016, MNRAS, 460, 2453
Smee S. A. et al., 2013, AJ, 146, 32
Smith A. et al., 2020, MNRAS, 499, 269
Sridhar S. et al., 2020, preprint (arXiv:2005.13126)
Sugai H. et al., 2012, in McLean I. S., Ramsay S. K., Takami H., eds, Proc. SPIE Conf. Ser. Vol. 8446, Ground-based and Airborne Instrumentation for Astronomy IV. SPIE, Bellingham, p. 84460Y
Takada M. et al., 2014, PASJ, 66, R1
Tamone A. et al., 2020, MNRAS, 499, 5527
Vargas-Magaña M. et al., 2018, MNRAS, 477, 1153
Wang Y. et al., 2020, MNRAS, 498, 3470
Weinberg D. H., Mortonson M. J., Eisenstein D. J., Hirata C., Riess A. G., Rozo E., 2013, Phys. Rep., 530, 87
York D. G. et al., 2000, AJ, 120, 1579
Zel'Dovich Y. B., 1970, A&A, 500, 13
Zhao C. et al., 2020a, preprint (arXiv:2007.08997)
Zhao G.-B. et al., 2020b, preprint (arXiv:2007.09011)

[1]*Institute of Physics, Laboratory of Astrophysics, Ecole Polytechnique Fédérale de Lausanne (EPFL), Observatoire de Sauverny, CH-1290 Versoix, Switzerland*
[2]*IRFU, CEA, Université Paris-Saclay, F-91191 Gif-sur-Yvette, France*
[3]*Center for Cosmology and AstroParticle Physics, The Ohio State University, Columbus, OH 43212, USA*
[4]*Institute for Astronomy, University of Edinburgh, Royal Observatory, Blackford Hill, Edinburgh, EH9 3HJ, UK*
[5]*Universidad Autónoma de Madrid, E-28049, Madrid, Spain*
[6]*Instituto de Fisica Teorica UAM/CSIC, Universidad Autonoma de Madrid, E-28049 Madrid, Spain*
[7]*Institute of Cosmology & Gravitation, University of Portsmouth, Dennis Sciama Building, Burnaby Road, Portsmouth PO1 3FX, UK*
[8]*Apache Point Observatory and New Mexico State University, PO Box 59, Sunspot, NM 88349, New Mexico*
[9]*University of Utah, Department of Physics and Astronomy, 115 S 1400 E, Salt Lake City, UT 84112, USA*
[10]*Waterloo Centre for Astrophysics, University of Waterloo, Waterloo, ON N2L 3G1, Canada*
[11]*Department of Physics and Astronomy, University of Waterloo, 200 University Ave W, Waterloo, ON N2L 3G1, Canada*
[12]*Kavli Institute for Particle Astrophysics and Cosmology, Stanford University, 452 Lomita Mall, Stanford, CA 94305, USA*
[13]*Max-Planck-Institut für extraterrestrische Physik (MPE), Giessenbachstrasse 1, D-85748 Garching bei München, Germany*
[14]*NSF's National Optical-Infrared Astronomy Research Laboratory, 950 N. Cherry Ave, Tucson, AZ 85719, USA*
[15]*Astrophysics Research Institute, Liverpool John Moores University, 146 Brownlow Hill, Liverpool L3 5RF, UK*
[16]*Aix Marseille Univ, CNRS, CNES, LAM, F-13388 Marseille, France*
[17]*Perimeter Institute, Waterloo, ON N2L 2Y5, Canada*
[18]*Department of Physics & Astronomy, Siena College, 515 Loudon Road, Loudonville, NY 12211, USA*
[19]*Department of Physics and Astronomy, University of Wyoming, Laramie, WY 82071, USA*
[20]*Department of Physics, University of Oxford, Denys Wilkinson Building, Keble Road, Oxford OX1 3RH, UK*
[21]*University of Pittsburgh and PITT PACC, Pittsburgh, PA 15260, USA*
[22]*Department of Physics and Astronomy, Ohio University, Clippinger Labs, Athens, OH 45701, USA*
[23]*Department of Physics and Astronomy, Sejong University, Seoul, 143-747, Korea*
[24]*Lawrence Berkeley National Laboratory, Berkeley, CA 94720, USA*
[25]*Department of Astronomy and Astrophysics, The Pennsylvania State University, University Park, PA 16802, USA*
[26]*Institute for Gravitation and the Cosmos, The Pennsylvania State University, University Park, PA 16802, USA*
[27]*Center for Cosmology and Particle Physics, Department of Physics, New York University, 726 Broadway, Room 1005, New York, NY 10003, USA*
[28]*School of Physics and Astronomy, University of St Andrews, North Haugh, St Andrews, KY16 9SS, UK*
[29]*Indian Institute of Astrophysics, Koramangala, Bangalore 560034, India*
[30]*National Astronomical Observatories of China, Chinese Academy of Sciences, 20A Datun Road, Chaoyang District, Beijing 100012, China*
[31]*University of Chinese Academy of Sciences, Beijing, 100049, China*

This paper has been typeset from a TEX/LATEX file prepared by the author.